Cell

Decoding Information in Cell Shape

Padmini Rangamani,[1,4] Azi Lipshtat,[1,5] Evren U. Azeloglu,[1] Rhodora Cristina Calizo,[3] Mufeng Hu,[2] Saba Ghassemi,[2] James Hone,[2] Suzanne Scarlata,[3] Susana R. Neves,[1] and Ravi Iyengar[1,*]
[1]Department of Pharmacology and Systems Therapeutics and Systems Biology Center, Icahn School of Medicine at Mount Sinai, New York, NY 10029, USA
[2]Department of Mechanical Engineering, Columbia University, New York, NY 10027, USA
[3]Department of Physiology and Biophysics, Stony Brook University, Stony Brook, NY 11794, USA
[4]Present address: Department of Molecular and Cellular Biology, University of California, Berkeley, Berkeley, CA 94720, USA
[5]Present address: Diagnostics, Simulations, and Software Department, Soreq NRC, Yavne 81800, Israel
*Correspondence: ravi.iyengar@mssm.edu
http://dx.doi.org/10.1016/j.cell.2013.08.026

SUMMARY

Shape is an indicator of cell health. But how is the information in shape decoded? We hypothesize that decoding occurs by modulation of signaling through changes in plasma membrane curvature. Using analytical approaches and numerical simulations, we studied how elongation of cell shape affects plasma membrane signaling. Mathematical analyses reveal transient accumulation of activated receptors at regions of higher curvature with increasing cell eccentricity. This distribution of activated receptors is periodic, following the Mathieu function, and it arises from local imbalance between reaction and diffusion of soluble ligands and receptors in the plane of the membrane. Numerical simulations show that transient microdomains of activated receptors amplify signals to downstream protein kinases. For growth factor receptor pathways, increasing cell eccentricity elevates the levels of activated cytoplasmic Src and nuclear MAPK1,2. These predictions were experimentally validated by changing cellular eccentricity, showing that shape is a locus of retrievable information storage in cells.

INTRODUCTION

Many cellular factors affect spatial dynamics of signaling. The presence of the lipid rafts in plasma membrane (Allen et al., 2007; Lingwood and Simons, 2010; Pike, 2009), cytoskeleton network (Ahmed et al., 2007; Allen et al., 2007; Deshpande et al., 2006; Iglic et al., 2006; Ten Klooster et al., 2006; Lacayo et al., 2007; Lingwood and Simons, 2010; Pike, 2009), scaffolding proteins (Allen et al., 2007; Lingwood and Simons, 2010; McMahon and Gallop, 2005; Pike, 2009; Westphal et al., 2000), and location of intracellular organelles (Ahmed et al., 2007; Campello and Scorrano, 2010; Deshpande et al., 2006; Freche et al., 2011; Iglic et al., 2006; Ten Klooster et al., 2006; Lacayo et al., 2007) all play important roles in controlling the spatial as well as temporal dynamics of signaling. But what about cell shape? It is well established that cell shape is controlled by both physical properties of the plasma membrane and the biochemical reactions involving membrane components and the underlying cytoskeleton, most often the actin filament network (Döbereiner et al., 2004; Dubin-Thaler et al., 2004, 2008; Giannone et al., 2007; Mogilner and Keren, 2009; Xiong et al., 2010). The intracellular signaling network activated by extracellular ligand binding to receptors in plasma membrane utilizes multiple signaling pathways containing small GTPases to regulate the actin cytoskeleton and thus control cell shape (Rangamani et al., 2011). So the shape of cells can be considered as a repository of information that flows through the cell signaling network. Is this information retrievable? If so, what could be the mechanisms of retrieval? These questions, although very fundamental in cell biology, also have translational relevance. For more than 100 years, the field of pathology has had as one of its major foci the observation of cell shape and tissue organization to identify disease states. This is done with precision, albeit in an empirical manner. If we were to understand how information in cell shape can be retrieved and utilized by cells, then there is the possibility that we can identify the mechanisms that relate cell shape to disease states.

The central hypothesis for this study is that cell shape can control signal transduction at the plasma membrane. By doing so, the information stored in cell shape can be retrieved and used to modulate cellular responses to extracellular signals. Such a hypothesis is impossible to answer solely by experimentation, as changing cell shape by plating cells on patterned surfaces affects cytoskeleton organization and dynamics (Ahmed et al., 2007; Allen et al., 2007; Deshpande et al., 2006; Iglic et al., 2006; James et al., 2008; Ten Klooster et al., 2006; Lacayo et al., 2007; Lingwood and Simons, 2010; Pike, 2009) that in turn regulate cell signaling. Hence, a theoretical approach is essential to determine whether cell shape can regulate signal transduction at the plasma membrane.

The fusiform shape is often associated with transformed cells. An early experimental study showed that cell shape controls proliferation (Folkman and Moscona, 1978). These experimental observations, in conjunction with our hypothesis, allowed us to formulate the following question: could the curvature of the plasma membrane result in the spatial gradients of activated signaling components in the plane of the membrane? To answer this question, we used reaction-diffusion formulations with homogeneous initial conditions and analyzed the effect of shape of the boundary on the spatial distribution of activated signaling components in the plane of the plasma membrane and subsequently in the cytoplasm as a function of time. We focused on ellipses as cell shapes because neoplastic transformation leads to cells acquiring a fusiform shape that is close to an ellipsoid (Figure S1 available online) (Campello and Scorrano, 2010; Kim et al., 1999; McMahon and Gallop, 2005). To determine whether cell shape by itself can modulate plasma membrane signal transduction, our mathematical model and numerical simulations did not include cytoskeletal regulation of membrane signaling or the presence of lipid rafts in the membrane. In the following sections, we briefly describe a mathematical model in both two and three dimensions and use it to generate numerical simulations and predictions. We then show that the predictions from the numerical simulations can be observed experimentally.

RESULTS

Mathematical Model for Membrane Gradients of Activated Signaling Components

Consider the following reaction, where A is a component in solution (extracellular or cytoplasmic component) and X is a membrane component. When A binds to X on the membrane, it forms B, which is also a membrane component. This is shown in Figure 1A.

$$A + X \underset{k_{off}}{\overset{k_{on}}{\rightleftharpoons}} B \qquad \text{(Equation 1)}$$

In the cytoplasm, A is free to diffuse. X and B are limited to the plasma membrane and are free to diffuse along the plane of the membrane. The dynamics of A in the cytoplasm are governed by

$$\frac{\partial C_A}{\partial t} = D_A \nabla^2 C_A \qquad \text{(Equation 2)}$$

where C_A is the concentration of A (in molecules/μm^3), and D_A is the diffusion coefficient (μm^2/s) of A.

The boundary condition accounts for the balance between diffusive flux and reaction rate at the boundary. This is given by

$$D_A(\mathbf{n} \cdot \nabla C_A) = -k_{on} C_A|_{\partial\Omega} N_X + k_{off} N_B \qquad \text{(Equation 3)}$$

where k_{on}, (μm^{3}s^{-1}molecules^{-1}) and k_{off} are the reaction rate constants (s^{-1}), N_X and N_B are the concentrations of X and B on the membrane, respectively (in molecules/ μm^2), $\mathbf{n}$ is the unit normal to the membrane at every point along the curve, and $C_A|_{\partial\Omega}$ is the concentration of A at the boundary.

Similarly, membrane components X and B satisfy the following equations

$$\frac{\partial N_X}{\partial t} = D_X \nabla^2 N_X - k_{on} C_A|_{\partial\Omega} N_X + k_{off} N_B \qquad \text{(Equation 4)}$$

$$\frac{\partial N_B}{\partial t} = D_B \nabla^2 N_B + k_{on} C_A|_{\partial\Omega} N_X - k_{off} N_B \qquad \text{(Equation 5)}$$

where D_X and D_B are the diffusion coefficients of X and B, respectively. Accordingly, N_X and N_B must satisfy periodic boundary conditions because the domain is closed. We assume that X has a uniform distribution in the membrane initially with a value N_{X0} (molecules/μm^2), and A has a uniform cytoplasmic distribution of C_{A0} (molecules/μm^3). Initially, the density of B is zero along the membrane.

We solved the above system of equations for a spherical and ellipsoidal geometry using separation of variables and analyzed the role of curvature in the generation of gradients of N_B in the plane of the membrane. The solution to the system of equations evolves similarly in both coordinates except the final form of the equations.

In many cases, only one surface of the cell is exposed to the stimulus. Therefore, simplification to a two-dimensional (2D) system is reasonable. For further simulations, we used the 2D geometry because it allows us to study the effect of curvature variation along a single axis. However, all results can be readily extended to three-dimensional (3D) models, and although the quantitative behavior of the membrane and cytoplasmic components may vary depending on the eccentricity and size of the ellipsoid, the angle-dependent wave function remains intact. In the case of a first-order reaction, we can obtain analytical solutions to the reaction-diffusion system as Mathieu functions in elliptic coordinates and Bessel functions (Arscott, 1964) in polar coordinates. We only show the final equations in the elliptical coordinates system here, and the complete derivation is in the Supplemental Information.

In elliptical coordinates, the final equations for radial and angular coordinates take the following form:

$$\frac{\partial^2 U}{\partial \mu^2} - (l - 2\omega \cosh(2\mu))U = 0 \qquad \text{(Equation 6)}$$

$$\frac{\partial^2 V}{\partial \nu^2} - (l - 2\omega \cosh(2\nu))V = 0 \qquad \text{(Equation 7)}$$

Here, $U(\mu)$ and $V(\nu)$ are the radial and angular functions for N_B, respectively; μ is the equivalent of the radius for the ellipse, and $\mu = \mu_0$ defines the ellipse; ν is the angle going from 0° to 360°. The quantities l and ω are given as

$$l = \left(a^2 \sinh^2 \mu_0 + \frac{a^2}{2}\right) \frac{\gamma D_A}{(D_A - D_B)} \qquad \text{(Equation 8)}$$

$$\omega = \frac{a^2 \gamma D_A}{4(D_A - D_B)} \qquad \text{(Equation 9)}$$

where a is the distance between the two foci of an ellipse, and γ is the effective reaction rate in spatial coordinates at the boundary (see Supplemental Information). Equations 6 and 7 are the modified Mathieu and the Mathieu differential equation, respectively (McLachlan, 1947). There is no analogous solution like the m = 0 (see Equation S33) mode for the angular dependence, $V(\nu)$. The solution to the Mathieu functions is a series summation of sines and cosines, and it inherently has an angular dependence. The solution to these equations was computed numerically.

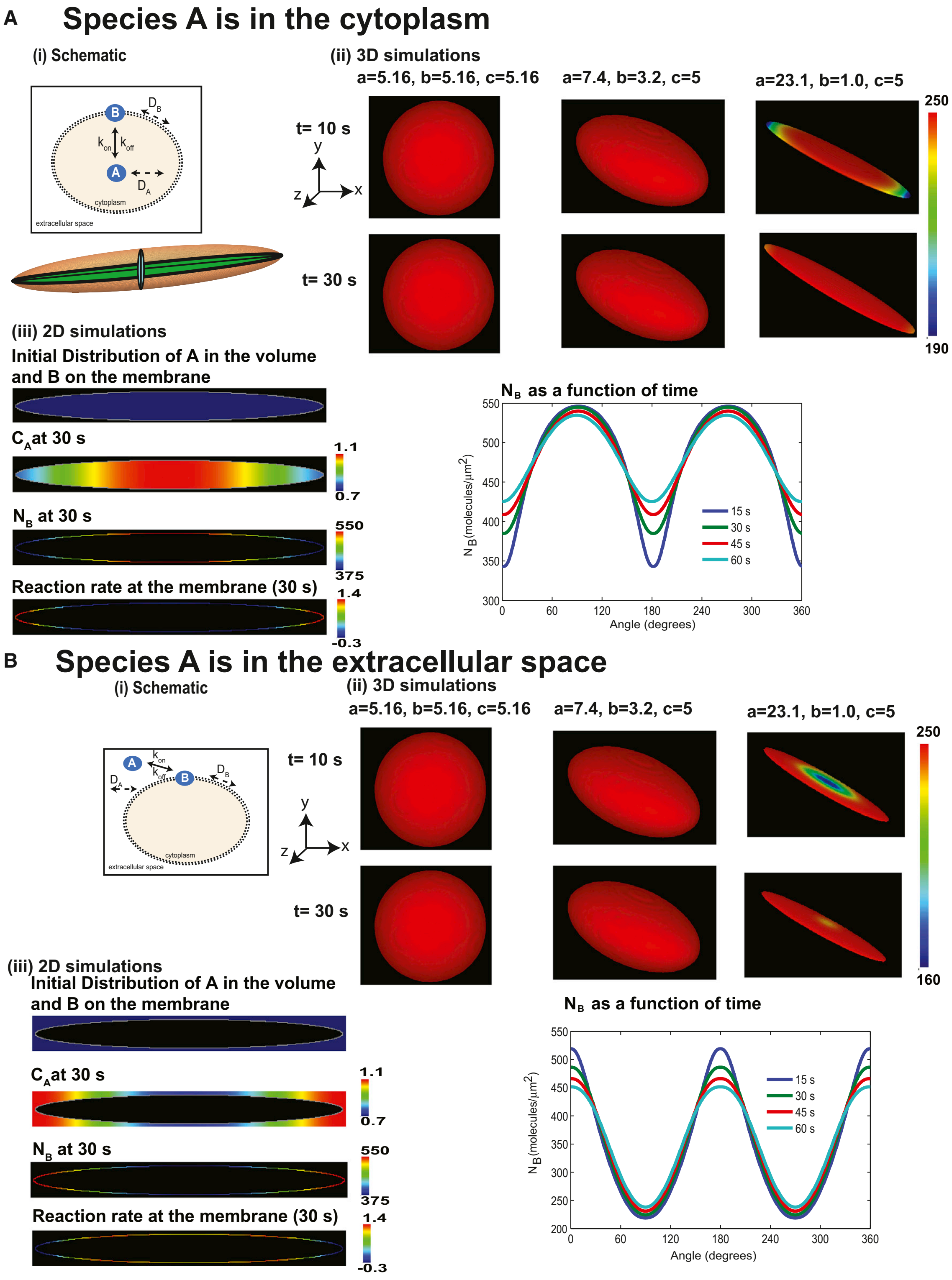

Figure 1. Simulations of the Effect of Membrane Curvature on the Transformation of Homogeneous Initial Distribution of Signaling Components to Transient Inhomogeneities in the Membrane and the Cytoplasm

(A) Signaling from the cytoplasm to the membrane. (i) The cytoplasmic component A binds to the plasma membrane to form membrane component B. A is free to diffuse in the cytoplasmic volume, whereas B has lateral mobility in the plane of the membrane. The cartoon below the reaction scheme illustrates that, in an ellipsoid, all 2D cross-sections passing through the center yield ellipses. (ii) Membrane surface distribution of B in 3D at 10 and 30 s in a sphere and two ellipsoids.

(legend continued on next page)

Numerical Simulations

Partial differential equations resulting from the reaction diffusion system were solved numerically using the Virtual Cell suite (Loew and Schaff, 2001). The volume component A can be present either in the cytoplasm (Figure 1A) or extracellular space (Figure 1B). In either case, interaction with the membrane depends on the local curvature. Therefore, we conducted simulations for two conditions: (1) when component A is in the cytoplasm (Figure 1A) and (2) when A is in the extracellular space (Figure 1B).

We conducted simulations using 3D geometries. When the volume component A is present in the cytoplasm, there is no spatial variation of membrane component B along the membrane for a sphere. However, as the eccentricity of the ellipsoid increases, the membrane distribution becomes curvature dependent at early times. In this case, the concentration of B is lower at the tip than at the body (Figure 1A, ii). In an ellipsoid, there are surface gradients along all three axes because every cross-section passing through the center of an ellipsoid is an ellipse (see Figure 1A, i, inset).

The system of equations for the 2D reaction-diffusion model was implemented using an elliptical geometry with eccentricity 0.999, and the concentrations of A and B were computed as a function of time (Figure 1A, iii). This geometry was chosen as it is similar in shape of elongated cells characteristics of those that have undergone neoplastic transformation (see Figures S1A–S1C) (Kalluri, 2009; Kalluri and Zeisberg, 2006; Young et al., 2006). At time zero, as per the initial conditions, C_A is homogeneous in the cytoplasm, and N_B is zero on the membrane (Figure 1A, iii). At 30 s, both C_A and N_B demonstrate a concentration gradient (Figure 1A, iii). Furthermore, the reaction flux also shows an angular dependence (Figure 1A, iii). The angular dependence of N_B varies in time during the course of the simulation (Figure 1C, v). The angular dependence of the membrane gradient is a result of the Mathieu functions. In fact, the first mode of the Mathieu sine function shows the same periodicity and qualitative behavior (McLachlan, 1947) as that of the membrane gradient of N_B.

When A is present in the extracellular space, the curvature dependence is reversed (Figure 1B). As expected, a spherical geometry does not exhibit any spatial variation of B along the membrane. As the eccentricity of the ellipsoid increases, the curvature-dependent gradients can be observed transiently (Figure 1B, ii). The membrane gradient exhibits a Mathieu cosine function (Figure 1B, iii). This is because the surface-to-volume relationships are reversed. Therefore, depending on the location of the volume component (cytoplasmic or extracellular), the regions of high curvature ($\theta = 0$) will have minimum or maximum concentration, respectively. We also tested whether the shape of the outer bounding box (similar to extracellular space) would affect the membrane pattern, and we see that, when A is present in the extracellular space (such as a ligand for a membrane bound receptor), the shape of the outer bounding box does not qualitatively affect the nature of the membrane gradient (Figure S1D).

When the reaction pathway is unidirectional toward the membrane—that is, extracellular ligand binding the receptor (Figure 1B) or the intracellular component binding the receptor (Figure 1A)—the effect of curvature is as described by the theoretical analysis. However, when both intracellular and extracellular components bind the membrane-bound receptor, the effect of curvature will depend on the relative rates of reaction and concentrations of the reactions (extracellular species $A \rightarrow$ membrane species $B \leftarrow$ intracellular species C). This effect can be explained by a simulation (Figure S1E) in which both an extracellular and a cytoplasmic component bind simultaneously (within our timescale) to the membrane. Because signal transduction at the cell surface almost always involves near-simultaneous binding of ligand to the receptor on the outer surface and cytoplasmic signaling components on the inner surface, we tested and found that simultaneous binding of cytoplasmic and extracellular components to the membrane can also result in curvature-dependent membrane gradients of B (Figure S1E). Thus, a homogeneous initial distribution can be converted into a signaling microdomain by the curvature of the membrane (i.e., cell shape). In addition to curvature, the directionality of the reactions is also important for curvature-dependent gradients of components restricted to the boundary (i.e., plasma membrane).

Mechanism Underlying Dynamics of Membrane Gradient of Signaling Components

Local Competition between Reaction and Diffusion

What is the physical basis for this differential distribution along the boundary (i.e., the plasma membrane)? The process of free diffusion works toward homogenizing concentration gradients; i.e., Fickian diffusion eliminates concentration gradients over a length scale. On the other hand, chemical reactions are occurring everywhere along the cell membrane, and the local surface-to-volume ratio establishes concentration differences along the membrane. The balance between these two processes is represented by the Thiele modulus (Φ), a dimensionless number. The Thiele modulus is used in chemical engineering to characterize processes that involve reaction diffusion on immobilized surfaces such as catalyst pellets. In those cases, the typical length scale is the size of the catalyst pellet. In the case of elliptical cell shapes, the radius of curvature is the natural choice for length scale. The radius of curvature, R_c, captures how curved the membrane is at any given point and is distinct from the distance from the center of the ellipse to the membrane. The radius of curvature is defined as the radius of the osculating circle that

The needle-shaped cell shows a transient spatial inhomogeneity in the membrane concentration of B. The dimensions of the shapes are shown on the panels. Initial concentration of A in the cytoplasm is 2 μM, and initial distribution of B on the membrane is 0 molecules/μm^2. The values of a, b, and c are the semiprincipal axes of the ellipsoid and determine its shape. For a sphere, a = b = c = radius of the sphere. (iii) Simulations of the distribution of signaling components in 2D geometry. Shown are the initial distribution of A (2 μM in the cytoplasm) and B (0 molecules/μm^2), concentration of A in the cytoplasm at 30 s, molecular density of B on the membrane at 30 s, and reaction rate along the membrane at 30 s, and angular dependence of membrane density of B at different times follows a Mathieu sine function.

(B) Same as in (A) except species A is in the extracellular space. The surface-to-volume relationship is reversed, and this results in a Mathieu cosine function. See also Figure S1.

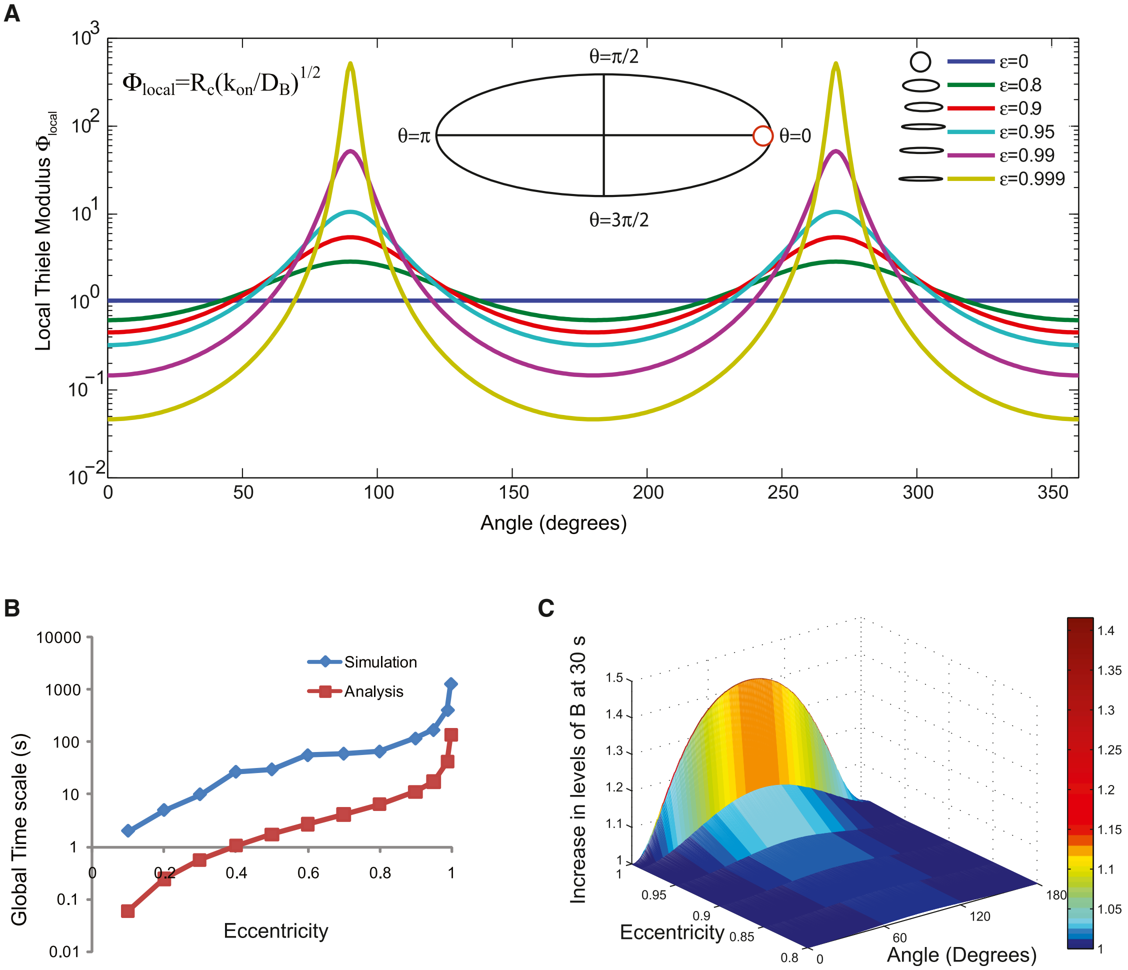

Figure 2. Angular Dependence of Local Thiele Modulus in Elliptically Shaped Cells

(A) Local Thiele modulus varies along the angle in an ellipse and results in competing reaction and diffusion processes along the membrane. The range of the local Thiele modulus also increases with increasing eccentricity of the ellipse. Inset shows a reference ellipse with the different angles marked. The red circle shows the osculating circle that determines the radius of curvature at the point θ = 0.

(B) The global timescales from analysis and numerical simulations follow similar dependence on eccentricity. Note that the simulation includes the timescale of the reaction, whereas the analysis is based on size and diffusivity alone.

(C) The fold change in component B along the membrane is calculated by normalizing the membrane concentrations by the value of B at θ = 0. The fold change in B depends on the eccentricity of the ellipse, and as the ellipse becomes more elongated (compare ε = 0.9 to ε = 0.999), the fold change in B increases.

can be drawn at each point along the curve; it is the inverse of curvature. At $\theta = 0$, the ellipse is highly curved, and a small circle (red circle in Figure 2A, inset) will fit in this circle. Hence, R_c is small here.

$$\Phi_{local} = R_c\sqrt{\frac{k_{on}}{D_B}} \qquad \text{(Equation 10)}$$

The competing processes of reaction and diffusion can be demonstrated by computing the local Thiele modulus (Equation 10 and Figure 2A). At $\theta = 0$, R_c is small, therefore Φ_{local} is small. Along the circumference of the cell, Φ_{local} varies from ~0.1, (a diffusion-limited regime) to >1,000 (a reaction-limited regime). Hence, the gradient of *A* in the cytoplasm follows the membrane gradient because closer to $\theta = 0$, reaction dominates, and closer to $\theta = \pi/2$, diffusion dominates.

As a result, the local reaction rate along the boundary depends on the local curvature (Figures 1A, iii, and 1B, iii). Consider $\theta = 0$ in Figure 2A; here, the local surface-to-volume ratio is high because curvature is high. Therefore, the contribution of reaction alone (per membrane unit area) is small—more *A* gets converted to *B* at the membrane, and there is a depletion of *A* in the local volume with a minor increase in N_B. In this local region, the process is diffusion limited because the reaction depletes *A* much faster than diffusion of *A* from the inside of the cytoplasm. In contrast, at $\theta = \pi/2$, the distance for *A* to travel from the center to the membrane is smaller; therefore, the process is less diffusion limited. When *A* is present in the extracellular space, the surface-to-volume ratio relationships are reversed (more at $\theta = 0$, less at $\theta = \pi/2$), and this is captured in the volume gradient of A, the membrane gradient of B, and the local reaction rate (Figure 1B).

Global Timescales and Effect of Eccentricity

How do the temporal characteristics of distribution at the boundary (i.e., plasma membrane) arise? The transient membrane inhomogeneities resulting from the shape of the cell are governed by a global timescale that captures the time required for the gradient to be abolished. We estimate the time required for gradient elimination as the difference between diffusion time at the major axis (r_1) and time at the minor axis (r_2) (Equation 11).

$$t = \frac{r_1^2 - r_2^2}{4D_A} \qquad \text{(Equation 11)}$$

The diffusion-limited "supply vs. demand" causes gradient formation, and thus the difference in diffusion times is a good indicator of the characteristic gradient relaxation time. We compare the computed timescale with the time required to achieve $N_B(\theta = 0) = N_B(\theta = \pi/2)$ in the simulations (Figure 2B) and see that the dependence of the timescale on eccentricity is similar. The simulation time includes reaction lifetime and diffusion time, although the analysis is only considering the diffusion.

In the case of a circle, the only acceptable mode of solution is when the mode number m is zero. This gives an exponential decay as the time-dependent solution (Equation S22). In elliptical coordinates, the mode numbers q (Equation S36) are not zero. They capture the different oscillatory patterns of the harmonic solutions of the Mathieu functions. Therefore, there are multiple contributions to the time-dependent solution. Each of these modes contributes to the final solution of the reaction-diffusion equation, and each mode converges to steady state with its own timescale. Areas that are closer to the zero point of the long-lasting modes would converge to steady state earlier than the others. As the eccentricity of the ellipse increases, more modes are required, and the significance of the different timescales increases. Because relaxation time increases dramatically with eccentricity, cell shape is a key determinant of how long the transient inhomogeneity will last along the membrane.

The increase in the concentration of N_B depends on the eccentricity of the ellipse (Figure 2C). As the eccentricity increases, the curvature range gets wider and the gradient gets steeper. Therefore, even if we start with the same concentration of a biochemical species at all locations, the shape of the cell will dynamically affect the spatial distribution of the activated signaling component in response to a membrane-delimited biochemical signaling event.

Model Predictions

Using our theoretical model, we make the following predictions that may be tested in numerical simulations and experiments. (1) A circular cell shape will have a homogeneous spatial activation of a membrane-bound receptor by a soluble ligand. Spatial distribution of activated receptor depends on the local curvature of the cell membrane. The persistence of a spatial gradient will depend on the relative rates of the reactions. (2) The transient spatial inhomogeneity at the plasma membrane can affect downstream reactions in a biochemical signaling pathway. As a result, there can be transient spatial gradients of the signaling components in the cytoplasm. (3) The effect of local curvature may also be seen in the cell nucleus. If the nucleus is elongated, then signaling interactions at the nuclear membrane will show an increase in activated signaling components in the nucleus.

In testing these predictions by numerical simulations, we had to introduce two additional details to make the simulations realistic: (1) we assumed near-simultaneous binding of agonist to receptor on the outside of the cell and recruitment of the appropriate signaling component from the cytoplasm and (2) inhomogeneous distribution of receptors as the starting condition, based on our observations described below, that receptors are present in higher density at the tips of elliptically patterned cells.

Numerical Simulations and Experimental Testing

GPCR

We simulated the distribution of the bradykinin receptor, a $G_{q/11}$-coupled receptor in circular and elliptical cells. We chose this receptor type because of the availability of good antibodies that allow us to study the native receptor in the cell. In response to activation by bradykinin, this receptor rapidly recruits β-arrestin (Gera et al., 2011; Philip et al., 2007). The lists of reactions, kinetic parameters, and diffusion coefficients are provided in Tables S1 and S2. As a starting point, we assumed that the initial distribution of the receptor was uniform (Figure 3A). Our simulations showed that, at early times after simulation, the receptors had a curvature-dependent distribution, with higher concentration on the cell body and lower concentration on the tip.

To test the predictions of this model, we manipulated cell shape by plating rat aortic smooth muscle A-10 cells on patterned surfaces that were either circular or elliptical. The plating of cells onto elliptical patterns always resulted in more receptors at the tip (Figure 3E). We then tested whether a nonuniform initial distribution (Figure 3B) as seen in the plated cells affected the spatial distribution of the receptor upon activation. We found that a similar curvature-dependent inhomogeneous receptor at early times after agonist addition could be seen, irrespective of the starting distribution (Figure 3B). Although we did not explore the causes of the initial inhomogeneous initial distribution, it is likely that this is related to plating in the presence of serum followed by serum starvation, a protocol that is essential for cells to adhere to the patterned surface. These predictions were tested experimentally in micropatterned A-10 cells (see Experimental Procedures).

The distribution of receptors in elliptical and circular cells is shown in Figures 3C and 3D. Experimental measurements of the receptor distribution in circular cells show that, before and after stimulation, the cells had a uniform distribution of receptors (Figure 3E). Experiments also showed that, in elliptical cells, the distribution of receptors prior to stimulation was nonuniform. The elliptical cells had higher receptor numbers at the tip than in the cell body. This is similar to the initial distribution shown in Figure 3B. One minute after stimulus, the elliptical cells showed a lower concentration of receptors in the tip than in the body (Figure 3E), similar to the predictions from the numerical simulations. We compared the ratio of receptor numbers in the cell tip to the

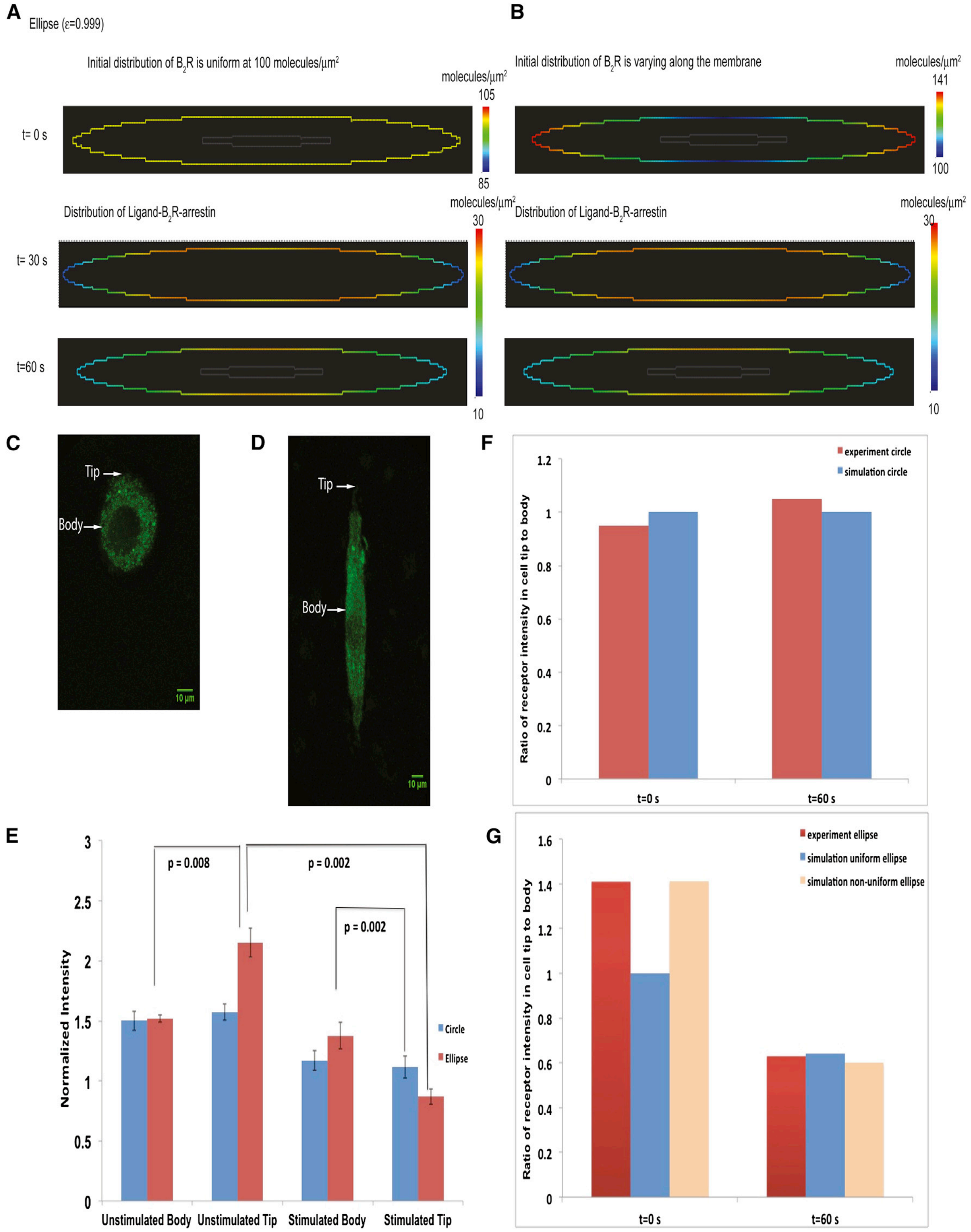

Figure 3. Numerical Simulations and Experiments on the Plasma Membrane Distribution of Bradykinin Receptor in Circular and Elliptical A-10 Cells

Simulation of the spatial distribution of active bradykinin receptor at 1 min for a uniform initial distribution. The concentration of active bradykinin receptor is higher in the body than in the tips. Please note that this simulation utilizes signaling components binding to the plasma membrane from both the outside (bradykinin) and inside (β-arrestin) of the cell (see Figure S1E).

(A) Simulation of the spatial distribution of active bradykinin receptor at 1 min for a nonuniform initial distribution of the receptor.

(B) Representative circular cell used for analysis. Arrows indicate the region of the plasma membrane where body and tip measurements were taken.

(C) Representative elliptical cell used for analysis. Arrows indicate the region of the plasma membrane where body and tip measurements were taken.

(legend continued on next page)

cell body in circular cells (Figure 3F) and elliptical cells (Figure 3G) and found a good match between model predictions and experimental observations.

Growth Factor Receptors

Growth factors such as epidermal growth factor (EGF) and platelet-derived growth factor (PDGF) activate the membrane-bound receptors, which results in downstream recruitment of adaptors such as SHC and the Grb2/Sos complex. Grb2/Sos is an adaptor-guanine nucleotide exchange factor complex for Ras and promotes the exchange of GDP for GTP on Ras leading to MAPK1,2 activation (Asthagiri and Lauffenburger, 2001; Bhalla et al., 2002; Fujioka et al., 2006; Hall, 2005). This pathway has been extensively modeled (Bhalla and Iyengar, 1999; Schoeberl et al., 2002). The complete set of reactions and parameters is presented in Tables S3, S4, and S5. The receptor activation by the ligand (present in the extracellular space) results in a membrane gradient with regions of high curvature having higher concentrations of ligand-bound activated receptor (Figure S1D). However, when the cytoplasmic components such SHC and Grb2/Sos bind the activated receptor, the regions of lower curvature now have a higher active EGFR concentration (Figures 4A and S1E).

When the initial membrane distribution of EGFR is uniform (Figure 4A), the active receptor shows transient curvature dependence, with higher receptor numbers at the cell body than at the tip. This effect is also observed when the initial distribution of EGFR is nonuniform as shown in Figure 4B. To test our prediction that activated growth factor receptor is in homogeneously distributed in a curvature-dependent manner, we conducted experiments using monkey kidney tissue-derived COS-7 cells that were grown to circular and elliptical shapes using microfabricated surfaces (see Supplemental Information). Most cells fully complied with the induced geometries and took ellipsoidal shapes (Figure S2). These cells were then transfected with EGFR-eGFP, and fluorescence correlation spectroscopy (FCS) was used to quantify receptor dynamics. Unstimulated cells showed a significant difference in the number of molecules (or concentration) between cell tip and body in elliptical cells (Figure 4E). Upon EGF addition to the cell medium, we observed an increased concentration of EGFR at the body and reduced concentration at the tips (Figures 4D and 4E). Circular cells showed no difference in receptor numbers in either control case or upon EGF addition (Figures 4C and 4E). Comparing the ratio of receptor number in the cell tip to cell body (Figures 4F and 4G) shows that the model predictions are validated by the experimental measurements.

Experimentally determined diffusion coefficients of EGFR between the body and the tip in stimulated elliptical cells differed significantly. A similar difference was also seen in tips before and after EGF stimulation (Figure S2E). Hence, we ran a set of simulations varying the diffusion coefficient of EGFR. In the experimentally observed range, we did not see a significant effect of diffusion coefficients on EGFR microdomains (Figure S3A). Because the levels of the transfected EGFR-eGFP are variable, we also ran a set of simulations to determine whether EGFR microdomains varied with overall receptor concentration. No significant effect was found in the experimentally observed range (Figure S3A).

The necessity of binding dynamics for the inhomogeneous distribution was tested by determining the distribution of a constitutively expressed yellow fluorescent protein (YFP)-labeled plasma membrane marker. When we measured the distribution of a YFP-labeled membrane marker (e-YFP-mem, Clontech), which is a doubly palmotiylated fusion protein containing residues 1–20 of GAP-43, no differences were found between circular and elliptical cells (Figures S2F and S2G). Overall, these simulations and experiments validate the first prediction from our mathematical analysis for two different types of membrane receptors.

The curvature-dependent transient gradient of EGFR on the membrane could have functional consequences for MAPK1,2 activation, which regulates gene expression in the nucleus to trigger cellular proliferation. We simulated the EGFR signaling pathway to MAPK1,2 activation and accumulation in the nucleus and explored the consequences of circular versus elliptical shapes. The concentration profiles of active Raf, MEK, and MAPK1,2 in the cytoplasm are greater in the elliptical cell shape than in the circular cell shape (Figure S4). We assumed elongated nuclear geometries in elongated cells because transformed cells have elongated nuclei (Dean et al., 2010).

The simulations show that the spatial distribution of MAPK1,2 in the cytoplasm (Figure 5A) and in the nucleus (Figure 5B) is nearly homogeneous because of the high diffusivity of MAPK in the cytoplasm. Further, average MAPK1,2 concentration in the nucleus and the concentration of MAPK1,2 in the cytoplasm are higher in the ellipse than in the circle (Figure 5C, i and ii). This is because the nuclear shape is elongated in the elliptical cell, which allows for a curvature-dependent reaction flux at the boundary of the cytoplasm-nucleus interface, similar to that at the extracellular space and the plasma membrane. The concentration of activated MAPK1,2 also depends on the eccentricity of the nucleus (Figure S4). In the ellipse, the activation of MAPK1,2 has a steeper initial increase when compared to the circle (Figure S5). The early increase in active MAPK1,2, combined with the increase in time for dissipation of gradient in an ellipse, can have a large impact on cellular decision-making processes even for small increases in the concentration of MAPK1,2. Therefore, transformed cells with the same number of growth factor receptors as normal cells can display enhanced levels of MAPK1,2 in the nucleus.

We experimentally tested the prediction that elliptical cells will show higher MAPK1,2 activity in the nucleus as compared to circular cells. Initially, we did this in live-cell imaging experiments. For this, COS-7 cells were transfected with a MAPK1,2 Förster

(D) Experiments determining levels of bradykinin receptor in the body or tip of circular and elliptical cells (n = 5). The normalized fluorescence intensity is compared between circular cells and elliptical cells. Data ± SD are shown. p values indicate statistical difference according to Mann-Whitney tests.

(E) Ratio of receptor intensity in cell tip to cell body in circular cells.

(F) Ratio of receptor intensity in cell tip to cell body in elliptical cells.

See also Tables S1 and S2.

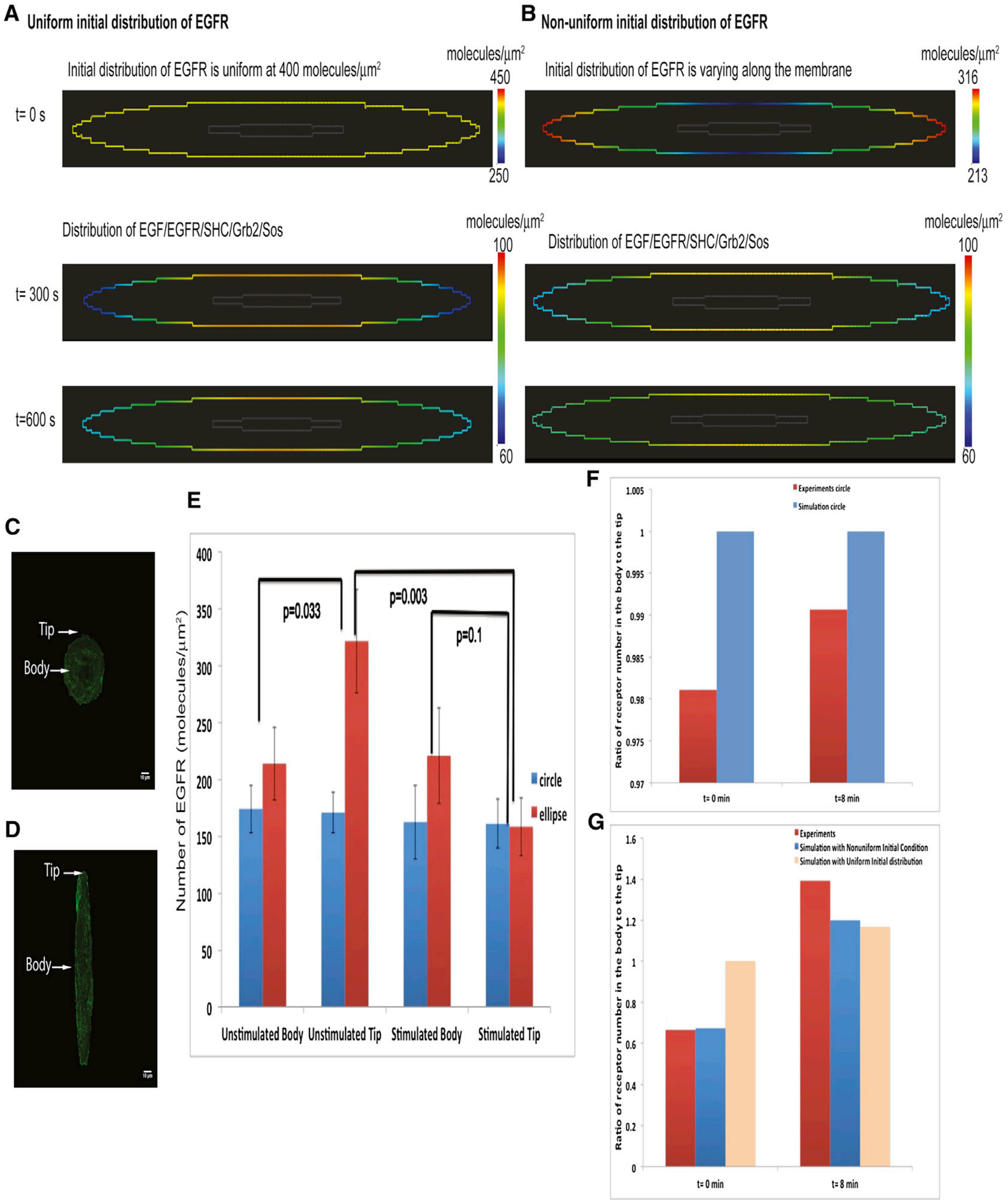

Figure 4. Numerical Simulations and Experiments on the Membrane Distribution of EGFR-eGFP in Circular and Elliptical COS-7 Cells

(A) Simulation of the spatial distribution of active EGFR-eGFP at 5 and 10 min. The concentration of EGFR is higher in the body than in the tips. Please note that this simulation utilizes signaling components binding to the plasma membrane from both the outside (EGF) and inside (SHC and GRB2) of the cell (see Figure S1E). The initial distribution of EGFR is uniform in this case.

(B) Simulations of the spatial distribution of active EGFR-eGFP at 5 and 10 min. The initial distribution of EGFR is nonuniform in this case. The concentration of EGFR is higher in the body than in the tips.

(C) Representative circular cell transfected with EGFR-eGFP. Arrows indicate the region of the plasma membrane where body and tip measurements were taken.

(D) Representative elliptical cell used for FCS analysis. Arrows indicate the region of the plasma membrane where body and tip measurements were taken.

(E) Experiments determining levels of EGFR-eGFP in the body or tip of elliptical cells (n = 14). Numerical values were extracted from the autocorrelation function fit to fluorescence correlation data for unstimulated data. Cells were measured after 12 hr of serum starvation; for stimulated data, measurements were started immediately after addition of 100 ng/ml EGF and were completed within 8 min. Data ± SD are shown. p values indicate statistical difference according to Mann-Whitney tests.

(F) Ratio of receptor number at the tip to body in simulations and experiment in circular cells.

(G) Ratio of receptor number at the tip to body in simulations and experiment in elliptical cells.

See also Figures S2 and S3 and Tables S3, S4, and S5.

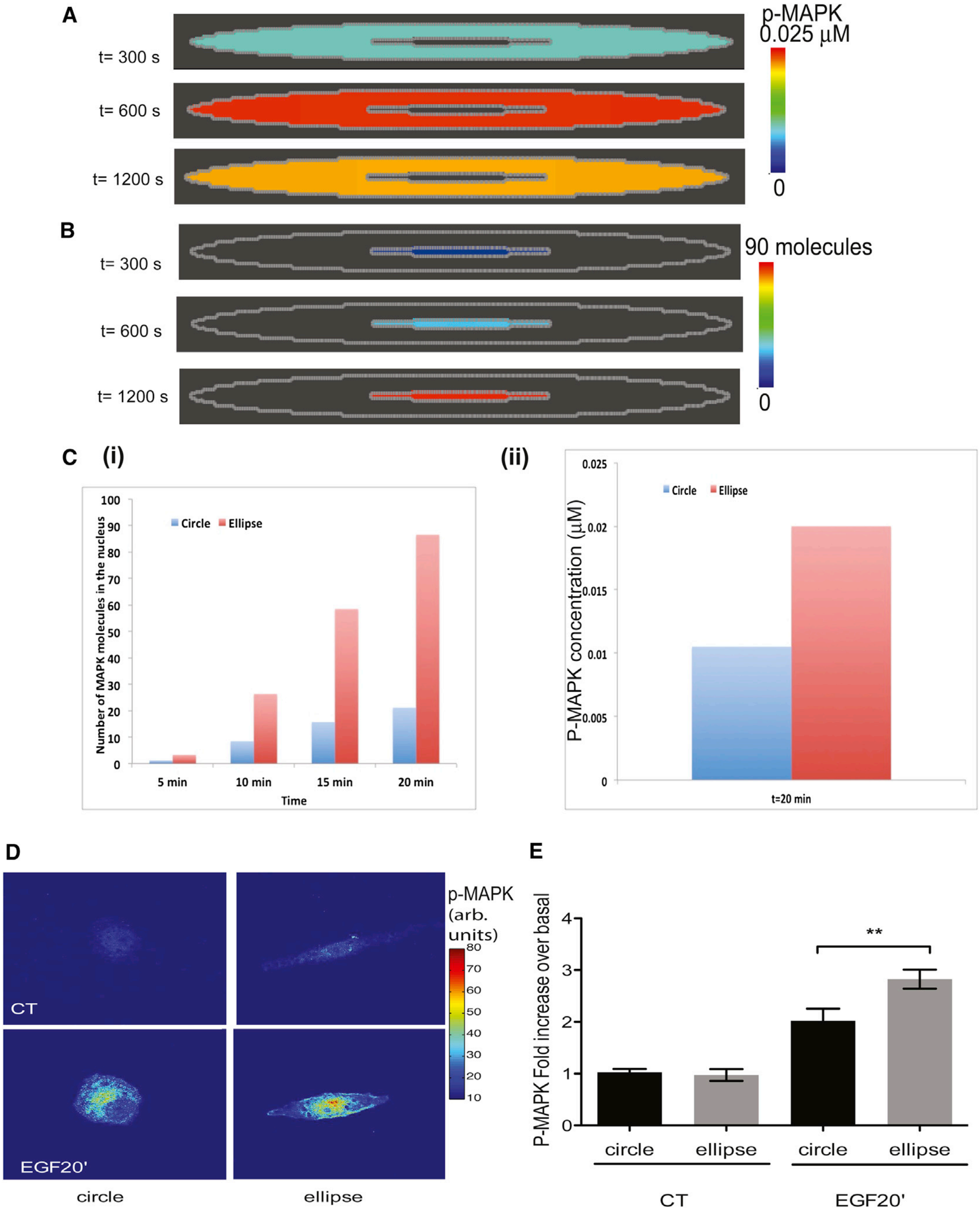

Figure 5. Levels of Activated MAPK1,2 in the Nucleus of Circular and Elliptical Cells

(A) Simulations of the activation of MAPK1,2 in the cytoplasm. The concentration of MAPK1,2 in the cytoplasm follows the kinetics shown in Figure S4—first increasing and then attaining a steady value before decreasing. The spatial distribution of MAPK1,2 in the cytoplasm appears uniform because of the high diffusion coefficient of MAPK1,2 in the cytoplasm. Later time points are shown for comparison with experiments

(B) Simulations of active MAPK1,2 in the nucleus. The concentration of MAPK1,2 increases with time in the nucleus. The spatial distribution of MAPK1,2 in the nucleus appears uniform because of the high diffusion coefficient of active MAPK within the nucleus.

(C) (i) From simulations, the number of molecules of active MAPK1,2 in the nucleus is higher in elliptical cells when compared to the number of active MAPK in circular cells. (ii) The concentration of p-MAPK1,2 in circular and elliptical cells at 20 min is shown from simulations.

(D) Elliptical COS7 cells stimulated with EGF show an enhanced accumulation of phosphor- MAPK. p MAPK1,2 immunostained cells are shown as color-coded grayscale images. Original pseudocolored images are shown in Figure S5.

(E) EGF-treated cells show a higher concentration of p-MAPK1,2 in elliptical cells than in circular cells. Fluorescence intensity ratios of nuclear p-MAPK1,2/ MAPK1,2 were plotted as mean ± SEM (n = 15–31; p = 0.0069; one-tailed t test)

See also Figures S4 and S5.

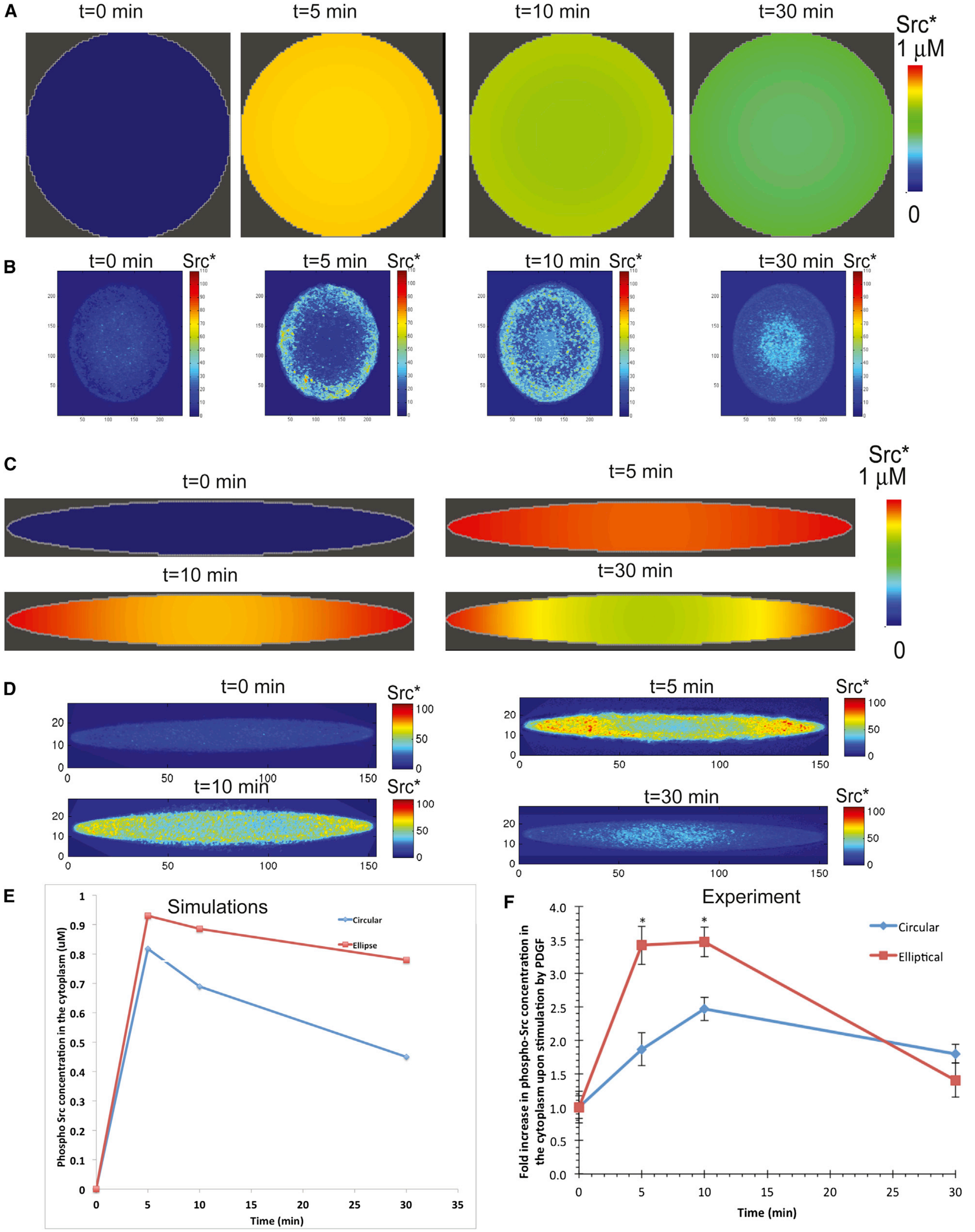

(legend on next page)

resonance energy transfer (FRET) probe that localizes to the nucleus (Harvey et al., 2008) and were plated on coverslips with microfabricated circular and elliptical wells. The cells were serum starved overnight and then stimulated with EGF, and activated nuclear MAPK1,2 response was measured using FRET. We found that, in elliptical cells, there was an increase in the level of activated MAPK1,2 in the nucleus compared to circular cells (Figure S5). However, these experiments were problematic because the cells transfected with the FRET probe that functions as a de facto dominant negative and plating on the engineered surfaces resulted in a large number of unhealthy cells, leading to variable responses (Figure S5, inset). Hence, we decided to use an immunochemistry approach in which cells plated on microfabricated surfaces were stimulated, fixed, and then stained with phospho-MAPK1,2 antibodies. This approach yielded much more reproducible observations. The nuclei of elongated cells had significantly higher amounts of phospho- to total-MAPK1,2. Representative pseudocolored images are shown in Figure 5D, along with the quantification of the average response in Figure 5E. The original images of the experiment in Figure 5D are in Figure S5. We show that this increase in nuclear MAPK1,2 activation is not due to changes in nuclear area (Figure S5).

To further establish the general relevance of our findings, we tested our model in another cell type, primary neonatal rat cardiac fibroblasts, where activation of Src is stimulated by the growth factor PDGF. Table S6 shows reactions and various parameters, and experimental time course of p-Src is shown in Figure S6. Whereas circular cells exhibit no spatial variation in Src activation at any time (Figure 6A), elliptical cells generate increased levels of activated Src at the tips where membrane curvature is also higher (Figure 6C).

In order to test these predictions experimentally, primary cardiac fibroblasts were grown on microfabricated surfaces, which resulted in cells with elliptical (eccentricity = 0.99) or circular (eccentricity = 0) shapes. Circular fibroblasts did not exhibit any spatial inhomogeneity of Src activation at any time (Figure 6B); elliptical cells, however, showed a curvature-dependent spatial activation of Src upon stimulation (Figure 6D). This spatial gradient lasted for up to 30 min, demonstrating that the local shape of the cell can induce transient spatial inhomogeneities on the activation of downstream signaling components.

Comparing the concentration of phospho-Src in the cytoplasm shows that elliptical cells have a higher concentration of phospho-Src than circular cells (Figure 6E). This behavior is also observed in experiments, in which elliptical fibroblasts show a higher concentration of phospho-Src when compared to circular cells (Figure 6F). In the case of Src, the cytoplasmic gradient is observed because Src may be associated with endosomal membranes and may not diffuse as fast as MAPK1,2 in the cytoplasm (Kaplan et al., 1992). Thus, the activation of Src through PDGF signaling also shows transient curvature dependence.

DISCUSSION

This study provides evidence that cell shape can play a role in information processing as extracellular signals are transduced to intracellular signals at the plasma membrane. This information-processing capability arises from simple reaction-diffusion kinetics of lateral mobility of proteins in the plane of the membrane and their ability to selectively interact with partners in the aqueous milieu either in the extracellular space, as is the case for receptor agonists, or intracellularly with components in the cytoplasm such as adaptors and exchange factors by receptor tyrosine kinases. Because receptor tyrosine kinases stimulate GTPases such as Rho, Rac, and Cdc42 to affect cell shape and because cell shape can in turn modulate receptor signals flowing through these GTPases, cell shape and growth factor signals can act as a multiscale feedback loop. Such feedback loops could play a role in reinforcing the transformed state, as rate of proliferation can depend on cell shape (Folkman and Moscona, 1978). Although the effects observed at the plasma membrane are small in magnitude, the propagation of these differences along the signaling pathway results in significant changes in downstream effectors such as Src and MAPK such that biologically meaningful effects are likely.

Using a combination of theory, numerical simulations, and experiments, we show that local curvature of the cell can modulate information processing of biochemical signaling pathways. The order of interaction between volume (extracellular and cytoplasmic) and surface (membrane-bound) components also plays an important role in determining the spatial pattern. As shown in Figure 1, in the simple case of one reaction, the resulting spatial gradient can be either Mathieu sine or cosine function. The local competition between reaction and diffusion combined with the reaction direction can lead to a transient inhomogeneity of membrane-bound components resulting solely from cell shapes. This conclusion obtained from our mathematical analyses and numerical simulations illustrates the nonintuitive knowledge of biological mechanisms that can be obtained from theoretical analysis.

Figure 6. Levels of PDGF-Activated Phospho-Src in Circle and Elliptically Shaped Cardiac Fibroblasts

(A) Simulations show that, in circular cells, homogeneous concentration of phospho-Src in the cytoplasm is obtained upon activation of the cells by PDGF.

(B) In experiments, circular cardiac fibroblasts grown in microfabricated grooves (n = 13–19) exhibit nearly uniform activation of Src near the plasma membrane, as measured by quantitative immunofluorescence.

(C) Simulations show that, upon activation, the concentration of phospho-Src leads to a curvature-dependent concentration gradient in the cytoplasm.

(D) In experiments, PDGF-activated phospho-Src in cardiac fibroblasts grown on elliptical cells (n = 12–14) shows a concentration gradient.

(E) Simulations show that phospho-Src in the cytoplasm has a higher concentration in elliptical cells when compared to the concentration of phospho-Src in circular cells.

(F) Summary of experimental data of fold increase of phospho-Src upon PDGF activation for indicated times. Values are means of 12–20 independent cells from two separate experiments and SEM (n = 12–20; $^*p < 0.001$ when comparing ellipses and circles at the same time point; unpaired two-tailed t tests with Bonferroni correction for multiple comparisons).

See also Figure S6 and Table S6.

The predictions from our model were tested experimentally in different cases. We tested the membrane distribution of receptors for bradykinin and EGF. In both cases, we were able to obtain a good match between the model prediction and the experimental observations. The net result of the curvature-dependent spatial inhomogeneity is that the concentration of downstream cytoplasmic component (MAPK1,2 and Src) is higher in elliptical cells than in circular cells. This observation provides one part of the explanation why cells that have undergone neoplastic transformation can have a higher MAPK activity.

The composition of the plasma membrane is complex, containing regional inhomogeneities in phospholipid and cholesterol concentrations (Eggeling et al., 2009; Lingwood and Simons, 2010) that will alter the lateral mobility of proteins. Additionally, the presence of membrane scaffolds and anchors that connect membrane proteins to the cytoskeleton will also affect lateral mobility. Given these regulatory processes, it would not be possible to fully experimentally decipher what, if any, contribution cell shape alone can make to information processing. The mathematical analyses and numerical simulations shown here clearly demonstrate that the simple physico-chemical properties of the system can enable cell shape to dynamically control information processing as signal flows across the cell-surface membrane. Because cell shape is often the result of prior signaling, in addition to network regulatory motifs such as positive-feedback loops (Bhalla and Iyengar, 1999), cell shape can also be considered a locus of information storage within the cell.

EXPERIMENTAL PROCEDURES

Microfabrication

Circular or elliptical wells were microfabricated with standard photolithography techniques (Qin et al., 2010). Briefly, glass coverslips were cleaned by successive washes in boiling 25% Linbro 7× surfactant and deionized water, nitrogen dried, and treated with oxygen plasma. They were then spin coated with a 500-nm-thick layer of SU-8 2000.5 resist, baked, exposed to UV light on a mask aligner, developed, and rinsed according to the manufacturer's instructions. The surface area for both elliptical and circular patterns was maintained constant at 2,000 μm^2. The circular patterns had a diameter of 50 μm. The major axis (r_1) and minor axis (r_2) for elliptical patterns was 134 and 19 μm, respectively.

Diffusion Measurements of EGFR-eGFP in COS-7 Cells

EGFR-eGFP is a kind gift from Dr. Linda Pike (Washington University School of Medicine). Micropatterned coverslips were pretreated with 500 μg/ml Gentamicin (Sigma) and 0.5% Pluronic F127 (Sigma) for 1 hr and washed with distilled water three times. Cells were reverse transfected with Fugene HD using manufacturer's instructions (Roche Diagnostics). Briefly, EGFR-eGFP and Fugene HD were complexed in a 1:3 μg DNA:μL Fugene ratio and incubated with ~70,000 COS-7 cells in suspension. 36 hr posttransfection, cells were incubated in serum-starving media (DMEM, 0.1% FBS) for 12 hr. At least 1 hr before stimulation, cells were treated with 10 mM NaN_3, 2 mM NaF, and 5 mM 2-deoxy-D-glucose to prevent internalization of EGFR (Liu et al., 2007).

Fluorescence correlation spectroscopy (FCS) measurements were performed on cells expressing EGFR-eGFP using a Zeiss LSM 510 Confocor-2 system equipped with 40× (N.A. 1.2) water immersion objective. eGFP was excited using 488 nm Argon laser, and the focal volume was determined using 10 nM Rhodamine 6G solution ($D = 2.8 \times 10^{-6}$ cm^2/s). The focal volume was focused on either the cell body, which was aligned with the nucleus, or on the cell tip, which was designated as within 5 μm from the apex of the cell shape (Figure S5A). A z axis scan of the cells showed two peaks corresponding to the basolateral and apical membrane populations of EGFR-eGFP (Figure S5B).

The apical peak was chosen for FCS measurements. Each FCS trace was measured for 20 s. EGFR was stimulated using 100 ng/ml of EGF. Measurements were started immediately after EGF addition and were completed within 8 min. Time traces that showed a decrease or increase of intensity were not used for analysis. Autocorrelation functions were analyzed using a two-component, pseudo-2D diffusion model by modifying the 3D fitting routine provided by the Confocor2 software and setting the structural parameter to quasi-infinite: $G(\tau) = 1 + 1/N\{(1+\tau/\tau_D)^{-1}[1+\tau(S^{-2}\tau_D)]^{-1/2}\}$, where τ is the correlation time, τ_D is the average time a particle spends in the confocal volume, N is the average number of molecules in the confocal volume, and S is the structural parameter, where S is set to 100 (quasi-infinite) for 2D diffusion. The diffusion coefficient, D, is calculated from the τ_D of a molecule using Einstein relation for diffusion: $r^2 = 4D \times \tau_D$, where r is the radius of the observation volume (Figure S2E). To quantify the number of EGFR-eGFP on the membrane, N was obtained from the fit, which is the average number of receptors in the confocal volume. To determine the concentration of receptors per unit area, N was divided by the area of the beam waist obtained through the calibration of the confocal volume with Rhodamine.

For details on mathematical modeling, simulations using Virtual Cell, the parameters used in the simulations, and standard experimental procedures please see the Supplemental Information.

SUPPLEMENTAL INFORMATION

Supplemental Information includes Extended Experimental Procedures, six figures, and six tables and can be found with this article online at http://dx.doi.org/10.1016/j.cell.2013.08.026.

ACKNOWLEDGMENTS

We thank Robert Blitzer, Marc Birtwistle, and the anonymous reviewers for very useful comments on the manuscript. We also thank T. Raymond Solano and Rumana Huq for their technical assistance. Primary cardiac fibroblasts were a kind gift from Dr. Kevin D. Costa; EGFR-eGFP was a kind gift from Linda Pike. This work was supported by NIH Grant (GM-072853 to R.I. and S.S.) and Systems Biology Center Grant (GM-071558). E.U.A. is a Howard Hughes Medical Institute Fellow of the Life Sciences Research Foundation. Confocal laser scanning microscopy was performed at the MSSM Microscopy Shared Resource Facility, supported with funding from NIH-NCI shared resources (5R24 CA095823-04), NSF Major Research Instrumentation (DBI-9724504), and NIH shared instrumentation (1 S10 RR0 9145-01) grants. Virtual Cell is supported by NIH grant P41-GM103313 from NIGMS. P.R. was supported by a fellowship from training grant (DK007645) from NIDDK.

Received: January 29, 2013
Revised: May 30, 2013
Accepted: August 14, 2013
Published: September 12, 2013

REFERENCES

Ahmed, I., Ponery, A.S., Nur-E-Kamal, A., Kamal, J., Meshel, A.S., Sheetz, M.P., Schindler, M., and Meiners, S. (2007). Morphology, cytoskeletal organization, and myosin dynamics of mouse embryonic fibroblasts cultured on nanofibrillar surfaces. Mol. Cell. Biochem. *301*, 241–249.

Allen, J.A., Halverson-Tamboli, R.A., and Rasenick, M.M. (2007). Lipid raft microdomains and neurotransmitter signalling. Nat. Rev. Neurosci. *8*, 128–140.

Arscott, F.M. (1964). Periodic Differential Equations: An Introduction to Mathieu, Lamé, and Allied Functions (New York: The Macmillan Company).

Asthagiri, A.R., and Lauffenburger, D.A. (2001). A computational study of feedback effects on signal dynamics in a mitogen-activated protein kinase (MAPK) pathway model. Biotechnol. Prog. *17*, 227–239.

Bhalla, U.S., and Iyengar, R. (1999). Emergent properties of networks of biological signaling pathways. Science *283*, 381–387.

Bhalla, U.S., Ram, P.T., and Iyengar, R. (2002). MAP kinase phosphatase as a locus of flexibility in a mitogen-activated protein kinase signaling network. Science *297*, 1018–1023.

Campello, S., and Scorrano, L. (2010). Mitochondrial shape changes: orchestrating cell pathophysiology. EMBO Rep. *11*, 678–684.

Dean, J.L., McClendon, A.K., Stengel, K.R., and Knudsen, E.S. (2010). Modeling the effect of the RB tumor suppressor on disease progression: dependence on oncogene network and cellular context. Oncogene *29*, 68–80.

Deshpande, V.S., McMeeking, R.M., and Evans, A.G. (2006). A bio-chemo-mechanical model for cell contractility. Proc. Natl. Acad. Sci. USA *103*, 14015–14020.

Döbereiner, H.G., Dubin-Thaler, B., Giannone, G., Xenias, H.S., and Sheetz, M.P. (2004). Dynamic phase transitions in cell spreading. Phys. Rev. Lett. *93*, 108105.

Dubin-Thaler, B.J., Giannone, G., Döbereiner, H.G., and Sheetz, M.P. (2004). Nanometer analysis of cell spreading on matrix-coated surfaces reveals two distinct cell states and STEPs. Biophys. J. *86*, 1794–1806.

Dubin-Thaler, B.J., Hofman, J.M., Cai, Y., Xenias, H., Spielman, I., Shneidman, A.V., David, L.A., Döbereiner, H.G., Wiggins, C.H., and Sheetz, M.P. (2008). Quantification of cell edge velocities and traction forces reveals distinct motility modules during cell spreading. PLoS ONE *3*, e3735.

Eggeling, C., Ringemann, C., Medda, R., Schwarzmann, G., Sandhoff, K., Polyakova, S., Belov, V.N., Hein, B., von Middendorff, C., Schönle, A., and Hell, S.W. (2009). Direct observation of the nanoscale dynamics of membrane lipids in a living cell. Nature *457*, 1159–1162.

Folkman, J., and Moscona, A. (1978). Role of cell shape in growth control. Nature *273*, 345–349.

Freche, D., Pannasch, U., Rouach, N., and Holcman, D. (2011). Synapse geometry and receptor dynamics modulate synaptic strength. PLoS ONE *6*, e25122.

Fujioka, A., Terai, K., Itoh, R.E., Aoki, K., Nakamura, T., Kuroda, S., Nishida, E., and Matsuda, M. (2006). Dynamics of the Ras/ERK MAPK cascade as monitored by fluorescent probes. J. Biol. Chem. *281*, 8917–8926.

Gera, L., Bawolak, M.T., Roy, C., Lodge, R., and Marceau, F. (2011). Design of fluorescent bradykinin analogs: application to imaging of B2 receptor-mediated agonist endocytosis and trafficking and angiotensin-converting enzyme. J. Pharmacol. Exp. Ther. *337*, 33–41.

Giannone, G., Dubin-Thaler, B.J., Rossier, O., Cai, Y., Chaga, O., Jiang, G., Beaver, W., Döbereiner, H.G., Freund, Y., Borisy, G., and Sheetz, M.P. (2007). Lamellipodial actin mechanically links myosin activity with adhesion-site formation. Cell *128*, 561–575.

Hall, A. (2005). Rho GTPases and the control of cell behaviour. Biochem. Soc. Trans. *33*, 891–895.

Harvey, C.D., Ehrhardt, A.G., Cellurale, C., Zhong, H., Yasuda, R., Davis, R.J., and Svoboda, K. (2008). A genetically encoded fluorescent sensor of ERK activity. Proc. Natl. Acad. Sci. USA *105*, 19264–19269.

Iglic, A., Hägerstrand, H., Veranic, P., Plemenitas, A., and Kralj-Iglic, V. (2006). Curvature-induced accumulation of anisotropic membrane components and raft formation in cylindrical membrane protrusions. J. Theor. Biol. *240*, 368–373.

James, J., Goluch, E.D., Hu, H., Liu, C., and Mrksich, M. (2008). Subcellular curvature at the perimeter of micropatterned cells influences lamellipodial distribution and cell polarity. Cell Motil. Cytoskeleton *65*, 841–852.

Kalluri, R. (2009). EMT: when epithelial cells decide to become mesenchymal-like cells. J. Clin. Invest. *119*, 1417–1419.

Kalluri, R., and Zeisberg, M. (2006). Fibroblasts in cancer. Nat. Rev. Cancer *6*, 392–401.

Kaplan, K.B., Swedlow, J.R., Varmus, H.E., and Morgan, D.O. (1992). Association of p60c-src with endosomal membranes in mammalian fibroblasts. J. Cell Biol. *118*, 321–333.

Kim, Y.S., Burns, A.L., Goldsmith, P.K., Heppner, C., Park, S.Y., Chandrasekharappa, S.C., Collins, F.S., Spiegel, A.M., and Marx, S.J. (1999). Stable overexpression of MEN1 suppresses tumorigenicity of RAS. Oncogene *18*, 5936–5942.

Lacayo, C.I., Pincus, Z., VanDuijn, M.M., Wilson, C.A., Fletcher, D.A., Gertler, F.B., Mogilner, A., and Theriot, J.A. (2007). Emergence of large-scale cell morphology and movement from local actin filament growth dynamics. PLoS Biol. *5*, e233.

Lingwood, D., and Simons, K. (2010). Lipid rafts as a membrane-organizing principle. Science *327*, 46–50.

Liu, P., Sudhaharan, T., Koh, R.M.L., Hwang, L.C., Ahmed, S., Maruyama, I.N., and Wohland, T. (2007). Investigation of the dimerization of proteins from the epidermal growth factor receptor family by single wavelength fluorescence cross-correlation spectroscopy. Biophys. J. *93*, 684–698.

Loew, L.M., and Schaff, J.C. (2001). The Virtual Cell: a software environment for computational cell biology. Trends Biotechnol. *19*, 401–406.

McLachlan, N.W. (1947). Theory and Application of Mathieu Functions (Oxford: Clarendon Press).

McMahon, H.T., and Gallop, J.L. (2005). Membrane curvature and mechanisms of dynamic cell membrane remodelling. Nature *438*, 590–596.

Mogilner, A., and Keren, K. (2009). The shape of motile cells. Curr. Biol. *19*, R762–R771.

Philip, F., Sengupta, P., and Scarlata, S. (2007). Signaling through a G Protein-coupled receptor and its corresponding G protein follows a stoichiometrically limited model. J. Biol. Chem. *282*, 19203–19216.

Pike, L.J. (2009). The challenge of lipid rafts. J. Lipid Res. *50*(Suppl), S323–S328.

Qin, D., Xia, Y., and Whitesides, G.M. (2010). Soft lithography for micro- and nanoscale patterning. Nat. Protoc. *5*, 491–502.

Rangamani, P., Fardin, M.-A., Xiong, Y., Lipshtat, A., Rossier, O., Sheetz, M.P., and Iyengar, R. (2011). Signaling network triggers and membrane physical properties control the actin cytoskeleton-driven isotropic phase of cell spreading. Biophys. J. *100*, 845–857.

Schoeberl, B., Eichler-Jonsson, C., Gilles, E.D., and Müller, G. (2002). Computational modeling of the dynamics of the MAP kinase cascade activated by surface and internalized EGF receptors. Nat. Biotechnol. *20*, 370–375.

Ten Klooster, J.P., Evers, E.E., Janssen, L., Machesky, L.M., Michiels, F., Hordijk, P., and Collard, J.G. (2006). Interaction between Tiam1 and the Arp2/3 complex links activation of Rac to actin polymerization. Biochem. J. *397*, 39–45.

Westphal, R.S., Soderling, S.H., Alto, N.M., Langeberg, L.K., and Scott, J.D. (2000). Scar/WAVE-1, a Wiskott-Aldrich syndrome protein, assembles an actin-associated multi-kinase scaffold. EMBO J. *19*, 4589–4600.

Xiong, Y., Rangamani, P., Fardin, M.-A., Lipshtat, A., Dubin-Thaler, B., Rossier, O., Sheetz, M.P., and Iyengar, R. (2010). Mechanisms controlling cell size and shape during isotropic cell spreading. Biophys. J. *98*, 2136–2146.

Young, B., Lowe, J.S., Stevens, A., and Heath, J.W. (2006). Wheater's functional histology: A text and colour atlas (Edinburgh: Churchill Livingstone).

Supplemental Information

EXTENDED EXPERIMENTAL PROCEDURES

Mathematical Model for Inhomogeneous Distribution of Activated Signaling Components in the Plane of Plasma Membrane

Consider the following reaction where A is a component in solution (extracellular or cytoplasmic component) and X is a membrane component. When A binds to X on the membrane, it forms B, which is also a membrane component. This is shown in Figure 1A.

$$A + X \underset{k_{off}}{\overset{k_{on}}{\rightleftharpoons}} B \qquad \text{(Equation S1)}$$

In the cytoplasm, A is free to diffuse. X and B are limited to the plasma membrane and are free to diffuse along the plane of the membrane. The dynamics of A in the cytoplasm are governed by

$$\frac{\partial C_A}{\partial t} = D_A \nabla^2 C_A \qquad \text{(Equation S2)}$$

where C_A is the concentration of A (in $molecules.\mu m^{-3}$), D_A is the diffusion coefficient ($\mu m^2/s$) of A.

The boundary condition takes into account that at the boundary the diffusive flux equals the reaction rate. This is given by

$$D_A(\mathbf{n} \cdot \nabla C_A) = -k_{on} C_A|_{\partial\Omega} N_X + k_{off} N_B \qquad \text{(Equation S3)}$$

where k_{on}, ($\mu m^3 s^{-1} molecules^{-1}$) and k_{off} are the reaction rate constants (s^{-1}), N_X and N_B are the concentrations of X and B on the membrane respectively (in $molecules/\ \mu m^2$), $\mathbf{n}$ is the unit normal to the membrane at every point along the curve, and $C_A|_{\partial\Omega}$ is the concentration of A at the boundary.

Similarly, membrane components X and B satisfy the following equations

$$\frac{\partial N_X}{\partial t} = D_X \nabla^2 N_X - k_{on} C_A|_{\partial\Omega} N_X + k_{off} N_B \qquad \text{(Equation S4)}$$

$$\frac{\partial N_B}{\partial t} = D_B \nabla^2 N_B + k_{on} C_A|_{\partial\Omega} N_X - k_{off} N_B \qquad \text{(Equation S5)}$$

Accordingly, N_X and N_B must satisfy periodic boundary conditions because the domain is closed. We assume that X has a uniform distribution in the membrane initially with a value N_{X0} ($molecules.\mu m^{-2}$), and A has a uniform cytoplasmic distribution of C_{A0} ($molecules.\mu m^{-3}$). Initially, the density of B is zero along the membrane.

We solved the above system of equations for a spherical and ellipsoidal geometry using separation of variables and analyzed the role of curvature in the generation of gradients of N_B in the plane of the membrane. The solution to the system of equations evolves similarly in both coordinates except the final form of the equations.

Separation of Variables

We use the separation of variables to write C_A as a function of time and space. As we will show, the spatial functions will depend on the coordinate system that is used. First, we write $C_A(\mathbf{r},t) = G(\mathbf{r})T(t)$, where $G(\mathbf{r})$ is the spatial and $T(t)$ is the temporal dependence. Equation 2 becomes

$$\frac{\dot{T}}{T} = D_A \frac{\nabla^2 G}{G} = -\lambda \qquad \text{(Equation S6)}$$

where λ is a separation constant. This leads to

$$T(t) = c_1 e^{-\lambda t} \qquad \text{(Equation S7)}$$

$$\nabla^2 G + \frac{\lambda}{D_A} G = 0 \qquad \text{(Equation S8)}$$

Eqn. S8 is the Helmholtz equation for the spatial dependence of C_A.

A Note on Coordinate Systems

The Helmholtz equation is separable in ten coordinate systems including confocal ellipsoidal and spheroidal coordinates (Arscott, 1964). These coordinate systems are ideal to study the simplified geometries that represent the shapes numerous cell type in normal (spheroidal) or neoplastically transformed (ellipsoidal) states (Figure S1). We can now solve the Helmholtz equation for the spatial dependence of C_A in multiple coordinate systems to understand how cell shape can affect the spatial distribution of A, X and B.

Spherical Coordinates

The spherical coordinate system is defined by (r, θ, φ), where $r \in [0, \infty]$, $\theta \in [0, \pi]$ and $\varphi \in [0, 2\pi]$.

$$r = \sqrt{x^2 + y^2 + z^2}, \theta = \cos^{-1}\left(\frac{z}{r}\right), \phi = \tan^{-1}\left(\frac{y}{x}\right) \qquad \text{(Equation S9)}$$

The spatial dependence can be further written using separation of variables as $G(\mathbf{r}) = R(r)\Phi(\phi)\Theta(\theta)$. The Helmholtz equation in Equation 8 becomes

$$\frac{r^2}{R}\frac{d^2R}{dr^2} + \frac{2r}{R}\frac{dR}{dr} + \frac{1}{\Theta}\frac{d^2\Theta}{d\theta^2} + \frac{\cos\theta}{\Theta \sin\theta}\frac{d\Theta}{d\theta} + \frac{1}{\Phi \sin^2\theta}\frac{d^2\Phi}{d\phi^2} + \frac{\lambda}{D_A}r^2 = 0 \qquad \text{(Equation S10)}$$

The above equation is separable and gives

$$\frac{1}{\Phi}\frac{d^2\Phi}{d\phi^2} = -m^2 \qquad \text{(Equation S11)}$$

which has a solution of the form

$$\Phi(\phi) = C_m \cos(m\phi) + D_m \sin(m\phi) \qquad \text{(Equation S12)}$$

The requirement for periodicity limits $2\pi m$ to integer values. Similarly, the r-dependent terms can be separated and equated to a constant

$$\frac{r^2}{R}\frac{d^2R}{dr^2} + \frac{2r}{R}\frac{dR}{dr} + \frac{\lambda}{D_A}r^2 = n(n+1) \qquad \text{(Equation S13)}$$

Multiplying throughout with R and solving the resulting spherical Bessel equation gives us

$$R(r) = A' j_n(kr) + B' n_n(kr) \qquad \text{(Equation S14)}$$

where $k = (\lambda/D_A)^{1/2}$, $j_n(kr)$ and $n_n(kr)$ are spherical Bessel functions of the first and second kind. This leaves us with the Θ terms that are dependent on both separation constants m and n.

$$\frac{d^2\Theta}{d\theta^2} + \frac{\cos\theta}{\sin\theta}\frac{d\Theta}{d}\theta + \left[n(n+1) - \frac{m^2}{\sin\theta}\right]\Theta = 0 \qquad \text{(Equation S15)}$$

The above equation is the associated Legendre differential equation for $h = \cos(\theta)$. The solution is given by associated Legendre functions, which play an important role in spherical harmonics. The solution does not diverge for non-negative integer values of n and for m values in the range $-n \leq m \leq n$. Furthermore, it can be shown through numerical methods that for any uniform initial distribution of A and X, the spatial distribution of B is uniform at all times (Figure 1).

Ellipsoidal Coordinates

The ellipsoidal coordinate system is given by α, β, γ as

$$\begin{aligned} & x = p^2 l sn(\alpha) sn(\beta) sn(\gamma), y = -p^2 l p'^{-1} cn(\alpha) cn(\beta) cn(\gamma), \\ & z = i l p'^{-1} dn(\alpha) dn(\beta) dn(\gamma) \end{aligned} \qquad \text{(Equation S16)}$$

where sn, cn and dn are Jacobi elliptic functions, l is a constant and p is the modulus of elliptic functions.

A complete derivation of the solution of the Helmholtz equation in ellipsoidal coordinates can be found in (Arscott, 1964). We present the key points here to highlight the evolution of the concentration gradient in the plane of the membrane. The ellipsoidal coordinate system is given by α, β, γ as defined in Eqn. S16. In these coordinates, the Laplacian is given by

$$\nabla^2 = \frac{\partial}{\partial x^2} + \frac{\partial}{\partial y^2} + \frac{\partial}{\partial z^2} = (H_1 H_2 H_3)^{-1} \sum_{\alpha,\beta,\gamma} \frac{\partial}{\partial \alpha}\left(\frac{H_2 H_3}{H_1}\frac{\partial}{\partial \alpha}\right) \qquad \text{(Equation S17)}$$

H_1, H_2 and H_3 are the scale factors. The Helmholtz equation (Eqn. S8) can now be separated in these new coordinates as $G(\alpha, \beta, \gamma) = A(\alpha)B(\beta)C(\gamma)$. The Helmholtz equation now reduces to

$$\sum_{\substack{\alpha,\beta,\gamma\\ A,B,C}} \left(sn^2(\alpha)-sn^2(\beta)\right)^{-1}\left(sn^2\gamma-sn^2\alpha\right)^{-1}\frac{A''(\alpha)}{A(\alpha)}-\frac{p^4l^2\lambda}{D_A}=0 \qquad \text{(Equation S18)}$$

Further simplification shows that $A(\alpha)$, $B(\beta)$ and $C(\gamma)$ satisfy the same equation of the type

$$\frac{d^2w}{dz^2}-\left(a+bp^2sn^2(z)+qp^4sn^4(z)\right)w=0 \qquad \text{(Equation S19)}$$

where one can solve for the arbitrary function $w(z)$ with a, b and q as parameters that depend on the separation constants.

This equation is the ellipsoidal wave equation. The solution to this equation is non-trivial and takes the form of ellipsoidal wave functions, which are doubly periodic. Therefore, $G(\alpha, \beta, \gamma)$ is a product of three ellipsoidal wave functions. The solution can only be constructed numerically (Arscott, 1981; Arscott and Darai, 1981) (Figures 1A and 1B, iii).

For simplicity, we assume that the membrane components X and B have the same diffusion coefficient, i.e., $D_X = D_B = D_N$. This allows us to have local conservation of X and B along the membrane. Then, the membrane density of B is given by

$$N_B=T(t)\frac{D_A(\mathbf{n}\cdot\nabla G)|_{\partial\Omega}+k_{on}G|_{\partial\Omega}N_{X0}}{k_{on}G|_{\partial\Omega}T(t)+k_{off}} \qquad \text{(Equation S20)}$$

Realistic cell shapes in three dimensions can be mathematically represented as ellipsoids. Our results can be easily extended to a 3-D system where they would be elliptical harmonic functions (Stratton, 1935a, 1935b). Consider the special case where the ellipse is rotated about its semi-minor axis to result in an oblate spheroid – the solution to the reaction-diffusion equation yields the *oblate spheroidal wave functions*. In contrast, when the ellipse is rotated about its semi-major axis, resulting in a prolate spheroid, the concentration distribution is given by *prolate spheroidal wave functions*.

Derivation of Mathieu Functions in Two Dimensions for Reaction-Diffusion Taking Place in Ellipsoidal Cell Shapes

Separation of Variables

We begin by analyzing the system in polar coordinates (r, θ, t), where r is the radial coordinate, $\theta \in [0, 2\pi]$, and t is time. Using separation of variables, we can write $C_A(r,\theta,t) = G(r)H(\theta)T(t)$ and Eqn. S4 becomes

$$\frac{\dot{T}}{T}=D_A\frac{\nabla^2(GH)}{(GH)}=-\lambda_{circle} \qquad \text{(Equation S21)}$$

Where λ_{circle} is a separation constant. This leads to

$$T(t)=c_1e^{-\lambda_{circle}t} \qquad \text{(Equation S22)}$$

$$\nabla^2(GH)+\frac{\lambda_{circle}}{D_A}(GH)=0 \qquad \text{(Equation S23)}$$

Eqn. S8 is the Helmholtz equation for the spatial dependence of C_A. The boundary condition (Equation 3) gives us

$$SD_AH(\theta)T(t)(\mathbf{n}\cdot\nabla G)|_{\partial\Omega}=-\frac{k_{on}}{S}G|_{\partial\Omega}H(\theta)T(t)+k_{off}N_B \qquad \text{(Equation S24)}$$

We then get

$$N_B(\theta,t)=\alpha_{circle}H(\theta)T(t) \qquad \text{(Equation S25)}$$

Where

$$\alpha_{circle}=\frac{\left(S^2D_A(\mathbf{n}\cdot\nabla G)|_{\partial\Omega}+k_{on}G|_{\partial\Omega}\right)}{(k_{off}S)}. \qquad \text{(Equation S26)}$$

Therefore, N_B is a projection of the angular and temporal dependence of C_A on the membrane scaled by α.

Using Eqn. S25 in Eqn. S21,

$$\frac{\dot{T}}{T}=D_B\frac{\nabla^2H}{H}-k_{off}+\frac{k_{on}G|_{\partial\Omega}}{S\alpha_{circle}} \qquad \text{(Equation S27)}$$

Define

$$\gamma_{circle} = -\left[\frac{k_{on}G|_{\partial\Omega}}{S\alpha_{circle}} - k_{off}\right] \tag{Equation S28}$$

Therefore,

$$\frac{\dot{T}}{T} + \gamma_{circle} = D_B\frac{\nabla^2 H}{H} = -\frac{m^2 D_B}{R_0^2} \tag{Equation S29}$$

where R_0 is the radius of the circle and must be an integer to satisfy the periodicity of the solution. This gives us

$$T(t) = T_0 e^{-\left(\gamma_{circle} + \frac{m^2 D_B}{R_0^2}\right)t} \tag{Equation S30}$$

Comparing Eqn. S5 and Eqn. S13, we get

$$\lambda_{circle} = \gamma_{circle} + \frac{m^2 D_B}{R_0^2} \tag{Equation S31}$$

The separation of G and H gives

$$r^2\frac{G''}{G} + r\frac{G'}{G} + \frac{\lambda}{D_A}r^2 = m^2 \tag{Equation S32}$$

$$\frac{H''}{H} = -m^2 \tag{Equation S33}$$

Therefore, we get a Bessel equation for $G(r)$ and an eigenvalue problem for $H(\theta)$. The initial distribution of C_A is homogeneous and therefore, the acceptable mode of the solution is *'m = 0'* resulting in homogeneous concentration profile in a circular domain.

Elliptical Coordinates

We use elliptical coordinates to solve the equations in an elliptical geometry. The coordinates are given by $x = a\cosh(\mu)\cos(\nu)$, $y = a\sinh(\mu)\sin(\nu)$, where *'a'* is the distance between the two foci of the ellipse, μ is an non-negative real number and $\nu \in [0, 2\pi]$; t is time. Using these coordinates, we write $C_A(\mu,\nu,t) = V(\nu)U(\mu)F(t)$ and we find that

$$\alpha_{ellipse} = \frac{\left(S^2 D_A(\mathbf{n}\cdot\nabla U)|_{\partial\Omega} + k_{on}U|_{\partial\Omega}\right)}{(k_{off}S)} \tag{Equation S34}$$

And

$$\gamma_{ellipse} = -\left[\frac{k_{on}U|_{\partial\Omega}}{S\alpha_{ellipse}} - k_{off}\right] \tag{Equation S35}$$

The equation for N_B becomes

$$\frac{\dot{F}}{F} + \gamma_{ellipse} = D_B\frac{V''(\nu)}{a^2(sinh^2(\mu_0) + sin^2(\nu))V(\nu)} = -q^2 \tag{Equation S36}$$

Furthermore, we can show that

$$\frac{\partial^2 U}{\partial\mu^2} - (l - 2\omega\, cosh(2\mu))U = 0 \tag{Equation S37}$$

$$\frac{\partial^2 V}{\partial\nu^2} + (l - 2\omega\, sinh(2\nu))V = 0 \tag{Equation S38}$$

Here

$$l = \left(a^2 \sinh^2 \mu_0 + \frac{a^2}{2}\right)\frac{\gamma D_A}{(D_A - D_B)} \tag{Equation S39}$$

$$\omega = \frac{a^2 \gamma D_A}{4(D_A - D_B)} \qquad \text{(Equation S40)}$$

and μ_0 is the value of μ at the boundary. Eqns. S37 and S38 are the Mathieu differential equation and modified Mathieu differential equation respectively. The solution of these equations results in the Mathieu sine and cosine functions.

Near-Simultaneous Binding of Cytoplasmic and Extracellular Volume Components to the Membrane

Most often signaling components bind to the plasma membrane from both the extracellular space and from the cytoplasm. A typical example is agonist binding to the transmembrane receptor on the extracellular surface. This binding event is almost instantaneously followed by recruitment of intracellular proteins such as scaffolds or other signaling molecules such as β-arrestin to the cytoplasmic surface of the agonist occupied receptor protein. In Figure S1, we show a simple model where an extracellular molecule (agonist) and a cytoplasmic molecule (e.g., scaffold) bind to the membrane (receptor) simultaneously. The resulting curvature dependence on the membrane depends on the relative rate of the binding reactions and the simulations are shown in the main paper Figures 3 and 4.

Using Virtual Cell Suite for Numerical Simulations

We used the Virtual Cell Suite for conducting the numerical simulations of the different biochemical signaling networks. The Virtual Cell framework is an intuitive and easy to use system for solving both ordinary and partial differential equations models representing biochemical reaction networks. Further, Virtual Cell models can incorporate in-plane diffusion of membrane species, a critical feature required for us to test the model in this study. The reaction network was specified using the physiology interface of the program and spatial applications were developed to solve the partial differential equations for the system. In addition to the reactions and the associated parameters, we specified the geometry associated with the system. Because the geometry was specified, the program was able to compute the compartmental volumes and sizes. As noted in the tables below, we also provided the diffusion coefficients for the different species. The partial differential equations model resulting from the different signaling networks contain different time scales (kinetics versus diffusion). We used the fully-implicit finite volume regular grid solver with variable time stepping to solve these systems equations. The finite volume method represents the partial differential equations as algebraic discretization equations at the mesh points, which exactly preserves the conservation laws. The time dependent solver used is the Sundials stiff solver CVODE. Because the time dependent solver is a stiff solver, it can handle multiple time scales that arise in the system of equations because of kinetics and diffusion. The relative error tolerance for time stepping was set to 10^{-7} and the absolute tolerance was set to 10^{-9}. The mesh for spatial discretization was set up such that the x element in the ellipse was 0.18 nm and the y element was 0.1 nm. This mesh size was determined based on convergence of the numerical solution. Making the mesh finer than this did not change the simulation results. All models described here are available publicly under public models by ‘prangamani’.

Simulation of Bradykinin Receptor Activation

The bradykinin receptor is a G protein coupled receptor and is coupled to $G_{q/11}$. Here we focus on a simple model of receptor activation by ligand binding. Upon ligand binding, G protein coupled receptors are phosphorylated almost immediately by G protein receptor kinase (GRK) and bound by β-arrestin (Lefkowitz, 1993; Liggett, 2011). A detailed model for GRK mediated regulation of GPCR signaling using the β2-adrenergic receptor system has been described (Vayttaden et al., 2010). Here, we only focus on the activation of the receptor by ligand binding and immediate downstream effects leading to β-arrestin binding. We have assumed the parameters of GRK and β-arrestin for the bradykinin receptors are the same as those for the β2-adrenergic receptors. The reactions, kinetic parameters, initial concentrations and the diffusion coefficients are shown in Tables S1 and S2.

Simulation of EGF Signaling in Circular and Elliptical Cells

The reactions and parameters used in this application are outlined in Tables S3, S4, and S5. We set up the reaction-diffusion simulations in the *Virtual Cell* suite. We then used a circle and ellipses of varying eccentricities to generate the geometries that were used in the simulations. In all the geometries, the cytoplasmic volume was maintained constant. The simulations shown in Figures 4 and 5 of the main text correspond to an ellipse of eccentricity 0.999. For the simulations that included the nucleus, we traced nuclei of different eccentricities (0.9, 0.99 and 0.999) within the ellipse of eccentricity 0.999 and mapped the location of nuclear MAPK to the nuclear domain. The nuclear concentration of active MAPK is shown as number of molecules. The ratio of cytoplasmic to nuclear volume was 13:1, similar to the value shown in (Fujioka et al., 2006) for Cos-7 cells. The ratio of nuclear to cytoplasmic volume varies depending on cell type. The conversion from μM to molecules in the nucleus was carried out as 1 μM = 600 molecules/μm^3 * 12 μm^3, where 12 μm^3 is the volume of the nucleus. We varied the ratio of cytoplasmic to nuclear volume (1:1, 3:1, 5:1) to investigate the effect of this ratio of nuclear MAPK activation (Figure S4). For these simulations, both the cell and the nucleus had eccentricities of 0.999. Decreasing the volume of the nucleus by increasing the ratio of cytoplasmic to nuclear volume reduced the number of active molecules of MAP kinase present in the nucleus.

In this model, MAPK is dephosphorylated in the cytoplasm by a protein tyrosine phosphatase (PTP). The nuclear transport (k_{in}) and efflux (k_{out}) of MAPK is modeled as a first order flux with an influx rate of 1.0 s^{-1} and efflux rate of 0.1 s^{-1} (Table S1). We do not include the MAPK phosphatase reaction in the model, which is why the concentration of active MAPK is high even at 1 hr. Inclusion of this loop may change the quantitative results of active MAPK concentration but will not change the qualitative effect of curvature on the concentration profile.

The simulations show that the average concentration of activated Raf in the cytoplasm is higher in the ellipse than in the circle (Figure S4A). The Raf cytoplasmic concentration differences are "transferred" to the downstream MEK activation (Figure S4B) and MAPK activation (Figure S4C). The advantage that the elliptical plasma membrane confers on the cytoplasmic MAPK activation is further enhanced by the inner nuclear boundary for an elliptical cell with elliptical nucleus (Figure S4D). Because most elongated cells appear to have elongated nuclei the amplification of the small differences in the cytoplasm is maintained from the curvature dependent plasma membrane gradient to the nuclear translocation. Thus, the physical shape of both the cell and the nucleus determine the overall processing capability of signal transferred from the extracellular space to the nucleus.

The cytoplasmic concentration of MAPK begins to asymptote toward its steady state value around 30 min or so (Figure S4C). The nuclear MAPK concentration on the other hand takes longer to reach steady state (Figure S4H) and this time depends in part on the ratio of k_{in} to k_{out}.

In the cytoplasm (Figures S4F and S4G), the gradients are minimal in the radial direction. This is because the diffusivity of MAPK in the cytoplasm is 7 $\mu m^2/s$ and active MAPK diffuses rapidly across the cytoplasm. The corresponding time scale for MAPK diffusion in the cytoplasm is given by $\tau = L^2/(4D_{MAPK*})$. In a circle, the length scale L is the radius (5 μm) and the corresponding length scale in the ellipse is the semi-major axis (23 μm). For the circular shape $\tau_{circle} < 1$ s and for the elliptical cell, $\tau_{ellipse} = 18.75$ s. This is why there is no observable cytoplasmic gradient at longer times (Figure S4G).

PDGF Stimulated Src Activation

If the effect of cell shape on propagation of signals in the cytoplasm is general, then curvature-mediated effects should be seen in different cell types. We simulated the phosphorylation of Src in the cytoplasm of cardiac fibroblasts. Table S6 provide the reactions and parameters for this system of reactions. The kinetic parameters for this set of reactions were varied to fit the time course of Src activation observed in experiments (Figure S6). The spatial distribution of active receptors is elliptical cells is shown in Figure S6. The cytoplasmic concentration of phospho-Src in these simulations is shown in Figure 6. Elliptical cells show a curvature dependent concentration of phospho-Src (Figure 6D), whereas circular cells do not show a curvature dependent activation profile of phospho-Src (Figure 6C).

Cell Culture

A-10 cell line (rat aortic smooth muscle cells) from ATCC and COS-7 monkey fibroblast cell line were maintained at 37°C in 5% CO_2 in DMEM (GIBCO) supplemented with 10% FBS (Gemini) and 1% Penicillin-Streptomycin (GIBCO).

Patterned coverslips were incubated with 0.5% Pluronic F127 for 3 hr. Coverslips were then washed and cells were plated in DMEM supplemented with 10% FBS. After 4-6 hr, cells were serum starved overnight in DMEM supplemented with 0.1% BSA.

Primary neonatal rat cardiac fibroblasts were a kind gift from Dr. Kevin D. Costa (Mount Sinai School of Medicine, New York, NY). Cells were isolated from P1-3 rats, grown in DMEM supplemented with 10% neonatal bovine serum and used within three passages.

FRET

Patterned cells were transfected with nuclear EKAR (1 μg) and lipofectamine 2000 (Invitrogen) in OPTI-MEM following manufacturer's instructions. After 4-6 hr, cells were serum starved with 0.1% BSA DMEM overnight. In a temperature controlled imaging chamber with recirculation, cells were imaged with a 40X objective in a Zeiss Axio Observer inverted microscope fitted with a QuantEM camera. Fluorophores were excited using a Colibri LED illumination system. CFP was illuminated with a 455 nm LED and a CFP cube (EX BP 436/25, BS FT 455, EM BP 480/40); YFP was excited with a 505 nm LED and a YFP cube (EX BP 500/25, BS FT 515, EM BP 535/30). FRET was monitored with the 455 nm LED and a FRET cube (EX BP 436/20, BS FT 455, EM BP 535/30). Fluorescence intensity ratios for FRET/CFP were plotted as a function of time.

Quantitative Imaging of Bradykinin-2 Receptor and Plasma Membrane Marker

A-10 cells which endogenously express Bradykinin 2 Receptor (B_2R)were seeded on the micropatterned coverslips which had been pre-treated with 0.5% pluronic, at a density of 70,000 cells/35-mm dish. Before fixing, cells were serum-starved for 12 hr in serum-starving media (DMEM, 0.1% FBS). Bradykinin-2 Receptor (B_2R) was stimulated with 0.1 μM bradykinin for 1 min. Cells were fixed for 20 min with 3% paraformaldehyde, 0.1% glutaraldehyde in phosphate buffered saline (PBS). Cells were then permeabilized with 0.2% Triton X-100 for 5 min and blocked with 3% bovine serum albumin. Cells were incubated with polycolonal anti-B_2R (Santa Cruz Biotech, sc-15050) at a concentration of 20 μg/ml for 48 hr at 4°C, followed by incubation with polyclonal Alexa 647 secondary antibody (Invitrogen) for 30 min. After washing, coverslips were mounted using Vectashield mounting media (Vector Laboratories).

To determine the distribution of a membrane marker, A10 cells were transfected with pEYFP-Mem (Clontech), which is a doubly palmitoylated fusion protein consisting of residues 1-20 of GAP43. Cells were transfected with Lipofectamine 2000 using manufacturer's instructions (Invitrogen). Briefly, 70,000 cells were incubated with the Lipofectamine-DNA complex at a ratio of 0.5 μg pEYFP: 1.5 μl Lipofectamine 2000 for 5 hr and then incubated in complete antibiotic free media (DMEM with 10% FBS). Transfected cells were detached and seeded on the micropattern coverslips after 24 hr and were allowed to attach to the micropattern for at least 18 hr. Cells were then fixed for 20 min with 3% paraformaldehyde, 0.1% glutaraldehyde in PBS.

Imaging was performed using Zeiss Concofor II confocal laser scanning microscope equipped with a 40x (N.A. 1.2) objective and 643 nm HeNe laser. Z-stack images were taken using a slice thickness of 0.5 μm.

Images were analyzed using ImageJ. Briefly, small regions of interest (ROIs) of the same size (0.7 μm circles) were selected on either the tip of the cell (within 5 μm from the cell tip) or the body of the cell (middle of the cell). This was done for over 10 ROIs. The intensities were averaged, and then normalized by dividing the average intensities of the region by the average intensity of the entire cell. Comparison of the normalized intensities was performed using Rank-sum test using SigmaPlot (Jandel Scientific, Inc.).

Quantitative Immunofluorescence

Cos-7 cells were stimulated with EGF (10 ng/ml) for 20 min and fixed with 4% paraformaldehyde supplemented with 4% sucrose. Cells were then permeabilized for 5 min with Triton-X and blocked with 5% normal goat serum (Vector Labs). Cells were incubated overnight with polyclonal anti-dually phosphorylated MAPK antibodies and monoclonal MAPK antibodies (Cell Signaling), followed by Alexa 488 or Alexa 564-conjugated secondary antibodies (Invitrogen). After washes, cells were counterstained with Hoechst 33259 (Invitrogen) and mounted using ProGold (Invitrogen). Fixed cells were imaged in a Zeiss Meta510 inverted confocal microscope using a 40X objective. Fluorophores were excited with an Argon laser at 488 nm, or HeNe at 543 nm. Hoechst dye was excited with a UV diode at 405 nm. 1024x1024 images were obtained. In ImageJ the Hoechst image was used to delimit the nuclear region. DIC was used to delimit the cell periphery.

Similarly, cardiac fibroblasts were serum starved overnight, stimulated with 10 ng/ml PDGF for 0, 5, 10 or 30 min, and rapidly fixed with 4% paraformaldehyde supplemented with 4% sucrose. They were then stained for phospho-Src using phospho-Y416 primary (Invitrogen) and Alexa 488-conjugated secondary antibodies as described above and imaged on a Leica SP5 DMI inverted laser scanning confocal microscope. Because all elliptical and circular cells had the same exact shape, and were imaged at the same time under same settings (both cell shapes were side-by-side on the same coverslip), the images of individual cells could be aligned and numerically averaged to produce a quantitative mean immunofluorescence intensity level for a given cell shape. Centroids of microfabricated wells were digitally aligned with the guidance of SU-8 resist autofluorescence (in the UV channel), and phospho-Src intensity (in the 488nm channel) for the entire well area was averaged (pixel-by-pixel) using Matlab (Mathworks, Natick, MA).

Parameters for Bradykinin Receptor Activation Pathway as Shown in Tables S1 and S2

The initial values of the Bradykinin receptor were assumed to be in the same range as the number of EGFR (see Figure 4). Arrestin is known to reduce the lateral mobility of GPCRs. The diffusion coefficient of B_2R was measured in (Philip et al., 2007). We used the smaller values of the diffusion coefficient for the arrestin bound receptor as discussed in (Philip et al., 2007; Slepak and Hurley, 2008). For the cytoplasmic components, we assumed a faster diffusion coefficient than the membrane components because of 3D diffusion.

Calculation of Diffusion Coefficients for Complex with EGFR as Shown in Table S5

The diffusivity of EGFR in the membrane is shown in Figure S2E. The molecular of EGFR is 134 kDa. Because EGFR dimerizes upon ligand binding, we use a molecular weight of 268 kDa as a standard for these calculations. The diffusivity of EGFR dimer was used from (Bhalla et al., 2002; Kholodenko et al., 1999). For calculating the membrane diffusivities of complexes of the adaptor proteins with Shc, we used the following relationship: diffusivity is inversely proportional to the square root of the molecular weight. We use the diffusivity of EGFR as the reference value and calculate the diffusivities as

$$\frac{D_1}{D_2} = \sqrt{\frac{M_2}{M_1}} \qquad \text{(Equation S41)}$$

For Ras, we assume that the addition of a phosphate in the GDP-GTP exchange does not modify the diffusivity in the plane of the membrane. For cytoplasmic components (Shc, Sos, Grb2, Ras-GAP), we used the diffusivity of MAP kinase (MW 42 kDa) as the reference and calculated their diffusivities based on the above formula.

Reactions and Parameters for PDGF Signaling

These reactions were developed based on Figure 2 of Bjorge et al. (2000) and also Roskoski (2005) and Storm et al. (1990). This set of parameters gave the best match with respect to experimental time scales of Src activation as shown in Figure 6F. Our goal was to match the time of maximal activation in particular.

SUPPLEMENTAL REFERENCES

Arscott, F. (1981). The land beyond Bessel: a survey of higher special functions. In Ordinary and Partial Differential Equations, W.N. Everitt and B.D. Sleeman, eds. (New York: Springer-Verlag), pp. 26–45.

Arscott, F.M., and Darai, A. (1981). Curvilinear co-ordinate systems in which the Helmholtz equation separates. IMA J. Appl. Math *27*, 33–70.

Bjorge, J.D., Jakymiw, A., and Fujita, D.J. (2000). Selected glimpses into the activation and function of Src kinase. Oncogene *19*, 5620–5635.

Kholodenko, B.N., Demin, O.V., Moehren, G., and Hoek, J.B. (1999). Quantification of short term signaling by the epidermal growth factor receptor. J. Biol. Chem. *274*, 30169–30181.

Lefkowitz, R.J. (1993). G protein-coupled receptor kinases. Cell *74*, 409–412.

Liggett, S.B. (2011). Phosphorylation barcoding as a mechanism of directing GPCR signaling. Sci. Signal. *4*, pe36.

Ljungquist-Höddelius, P., Lirvall, M., Wasteson, A., and Magnusson, K.E. (1991). Lateral diffusion of PDGF beta-receptors in human fibroblasts. Biosci. Rep. *11*, 43–52.

Lommerse, P.H., Vastenhoud, K., Pirinen, N.J., Magee, A.I., Spaink, H.P., and Schmidt, T. (2006). Single-molecule diffusion reveals similar mobility for the Lck, H-ras, and K-ras membrane anchors. Biophys. J. *91*, 1090–1097.

Mayawala, K., Vlachos, D.G., and Edwards, J.S. (2006). Spatial modeling of dimerization reaction dynamics in the plasma membrane: Monte Carlo vs. continuum differential equations. Biophys. Chem. *121*, 194–208.

Roskoski, R., Jr. (2005). Src kinase regulation by phosphorylation and dephosphorylation. Biochem. Biophys. Res. Commun. *331*, 1–14.

Sanghera, J.S., Paddon, H.B., Bader, S.A., and Pelech, S.L. (1990). Purification and characterization of a maturation-activated myelin basic protein kinase from sea star oocytes. J. Biol. Chem. *265*, 52–57.

Schmid, B., Schindelin, J., Cardona, A., Longair, M., and Heisenberg, M. (2010). A high-level 3D visualization API for Java and ImageJ. BMC Bioinformatics *11*, 274.

Seger, R., Ahn, N.G., Posada, J., Munar, E.S., Jensen, A.M., Cooper, J.A., Cobb, M.H., and Krebs, E.G. (1992). Purification and characterization of mitogen-activated protein kinase activator(s) from epidermal growth factor-stimulated A431 cells. J. Biol. Chem. *267*, 14373–14381.

Slepak, V.Z., and Hurley, J.B. (2008). Mechanism of light-induced translocation of arrestin and transducin in photoreceptors: interaction-restricted diffusion. IUBMB Life *60*, 2–9.

Storm, S.M., Cleveland, J.L., and Rapp, U.R. (1990). Expression of raf family proto-oncogenes in normal mouse tissues. Oncogene *5*, 345–351.

Stratton, J.A. (1935a). Spheroidal Functions of the Second Kind. Proc. Natl. Acad. Sci. USA *21*, 316–321.

Stratton, J.A. (1935b). Spheroidal Functions. Proc. Natl. Acad. Sci. USA *21*, 51–56.

Vayttaden, S.J., Friedman, J., Tran, T.M., Rich, T.C., Dessauer, C.W., and Clark, R.B. (2010). Quantitative modeling of GRK-mediated β2AR regulation. PLoS Comput. Biol. *6*, e1000647.

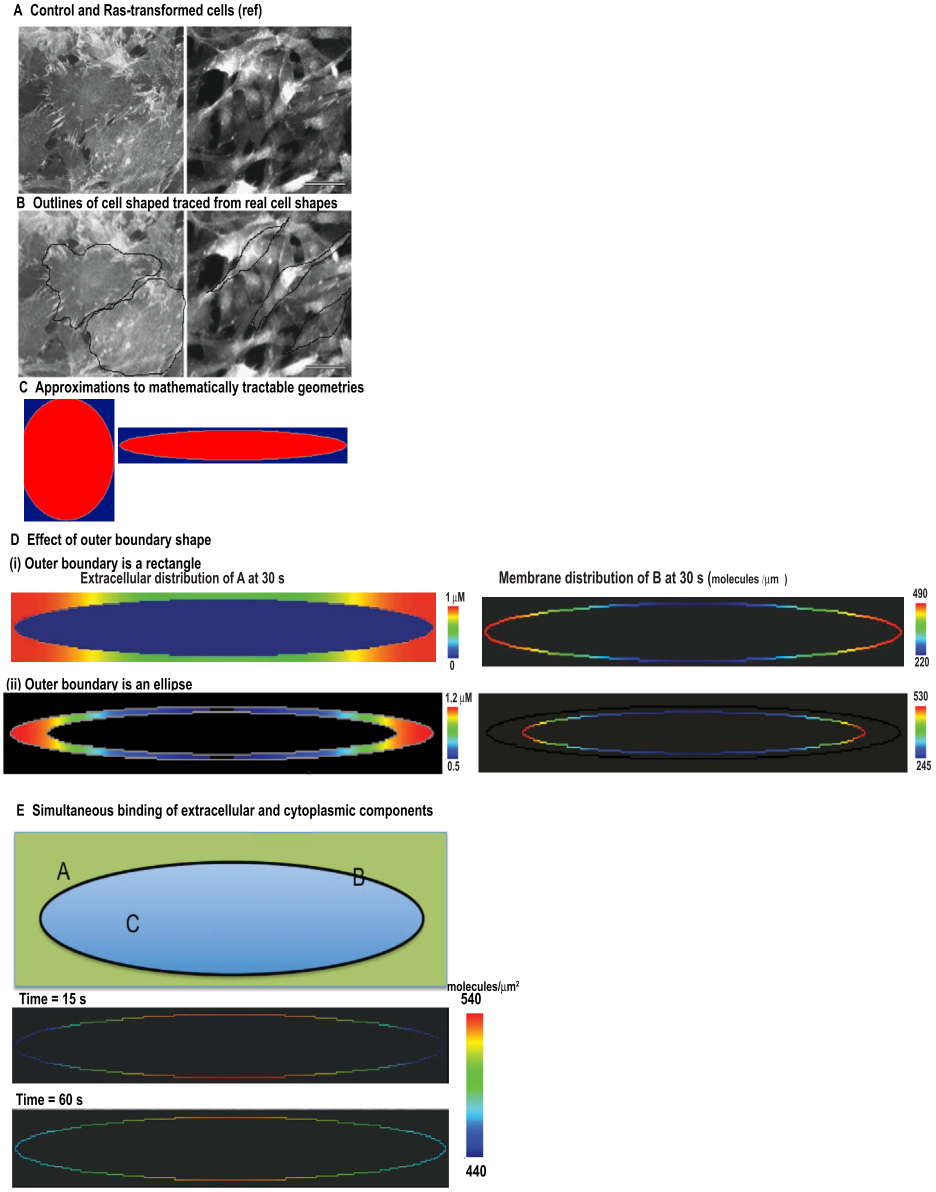

Figure S1. Geometry and Influence of Outer Boundary Shape, Related to Figure 1

(A) Original microscopy images from (*9*).

(B) Outlines are traced on the cell boundaries to obtain the cell shape. The scale bar on (A) and (B) is 50 µm.

(C) Idealized geometries approximated from (B) to obtain mathematically tractable shapes for analysis. The circle is 5 µm in radius and the major axis of the ellipse is 46 µm and minor axis is 2 µm. In all simulations, the area of the cell was held constant.

(D) Shape of the outer boundary does not affect the qualitative behavior of the membrane gradient. The elliptical cell is enclosed in an elliptical extracellular space of same eccentricity (0.999) but larger size. This extracellular shape is in comparison with that used in Figures 1A and 1B. The shape of the outer bounding box changes the concentrations quantitatively, but the angular dependence of the concentration of B does not change.

(E) Simultaneous binding of cytoplasmic and extracellular molecules to the membrane: when an extracellular molecule A binds to a membrane component and a cytoplasmic molecule C binds to the membrane component to form B, the relative rate constants can determine the regions where the concentration of B is high along the membrane. (i) Schematic of the locations of A, B and C, (ii) membrane concentration of B at 15 s and (iii) at 30 s.

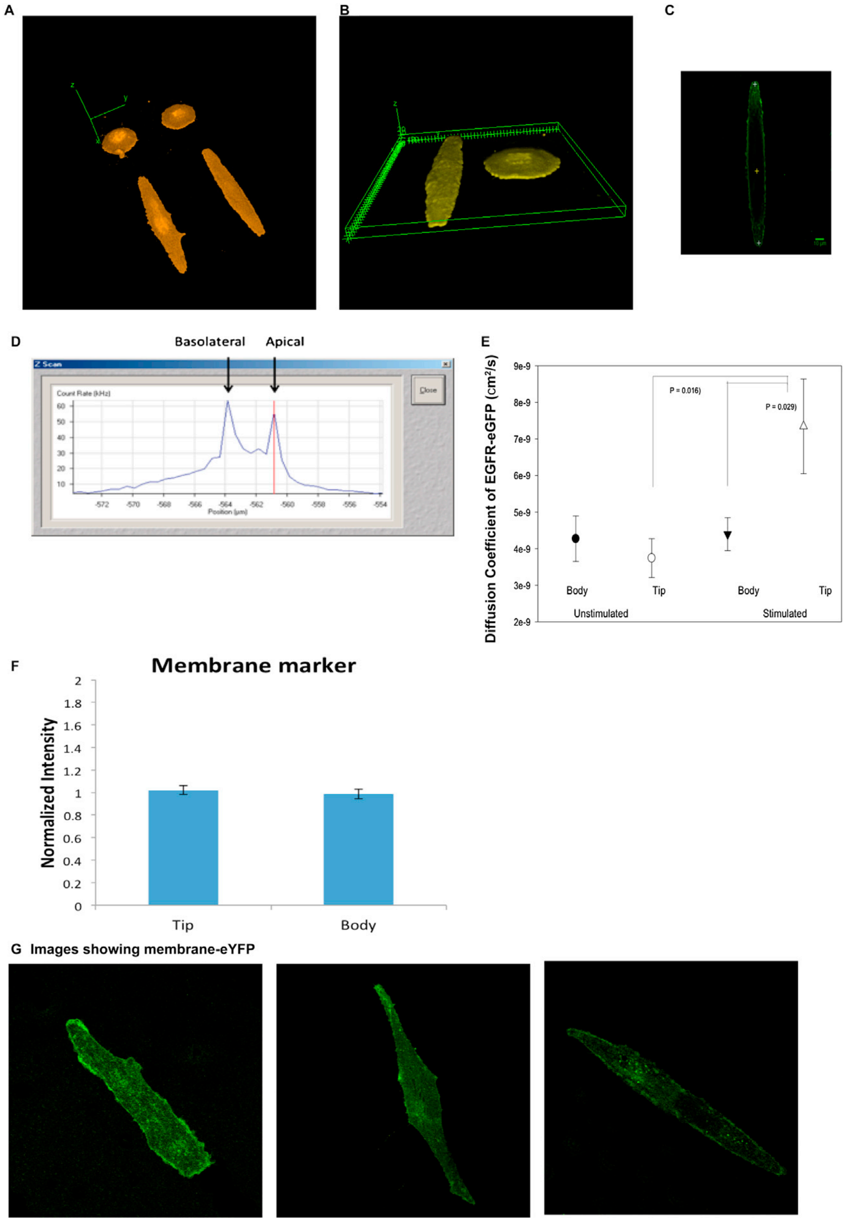

Figure S2. Experimental Measurements of EGFR Diffusivity, Related to Figure 4

(A and B) Top (A) and side (B) views of 3D reconstructions of fixed COS-7 cells expressing EGFR-eGFP. Confocal Z-stack images were obtained using Olympus Fluoview 1000 with optical sections of 0.5 µm. 3D reconstructions were performed using the ImageJ plugin, "3D Viewer" (Schmid et al., 2010).

(C) Diffusivity measurements of EGFR-eGFP in COS-7 cells. Representative image of COS-7 cells expressing EGFR-EGFP. Focal volumes for FCS measurements were centered on either cell body (designated as the median of the cell, yellow crosshair) or cell tip (1-5 µm from the apex of the cell, white crosshairs).

(D) Z-scan of a cell showing two peaks for both apical and basolateral membranes. The apical side was chosen for measurements.

(E) Diffusion measurements from FCS in stimulated and unstimulated elliptical cells. Data and SD are shown n = 14 for both unstimulated cells and stimulated cells for elongated cells.

(F) Distribution of membrane marker-eYFP in A10 cells. Comparison of normalized intensities of membrane marker-eYFP in A10 cells in the tip and body of ellipsoid cells. Data shown are average ± SEM (n = 10 cells).

(G) Representative images of ellipsoid cells showing the distribution of membrane marker-eYFP.

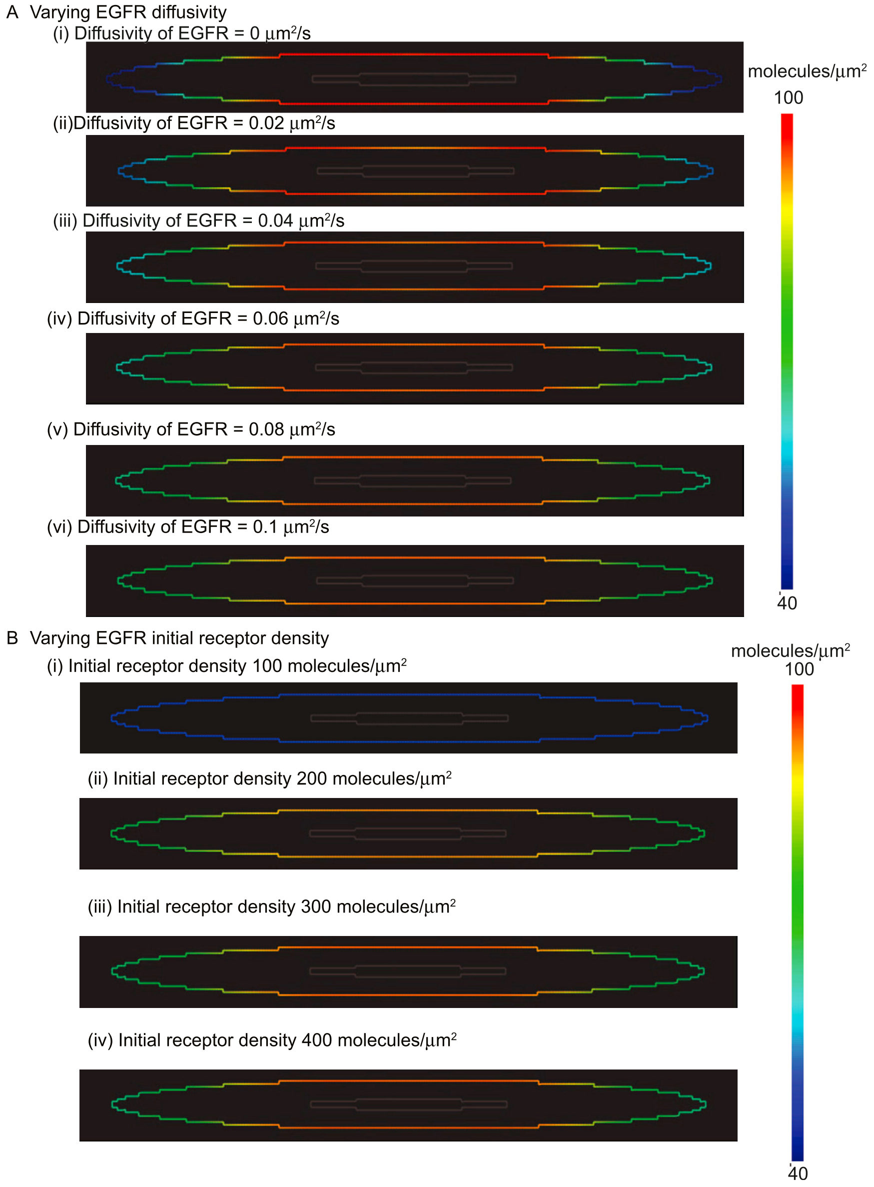

Figure S3. Effect of Varying Diffusion Coefficients and Initial Number of Receptors on EGFR Gradients in the Plane of the Membrane, Related to Figure 4

(A) We conducted simulations with different diffusion coefficients of EGFR based on the experimental observations. The different diffusion coefficients did not change the effect of membrane curvature on the receptor distribution. Increasing the diffusion coefficients decreased the difference between maximum and minimum values of the receptors on the membrane. The time required for the spatial distribution to homogenize was longer for smaller diffusion coefficients as calculated in Figure 2B.

(B) Because the receptor density often varies in cells (Figure 3C), we ran simulations with different receptor densities to determine the effect of receptor numbers on gradients in the plane of the membrane. The effect of curvature on local accumulation of receptors did not change above a threshold with different receptor densities. When the receptor density was low (100 molecules/μm^2, the spatial gradient of EGFR equilibrated by 300 s, see panel A). In all other cases gradients are clearly visible.

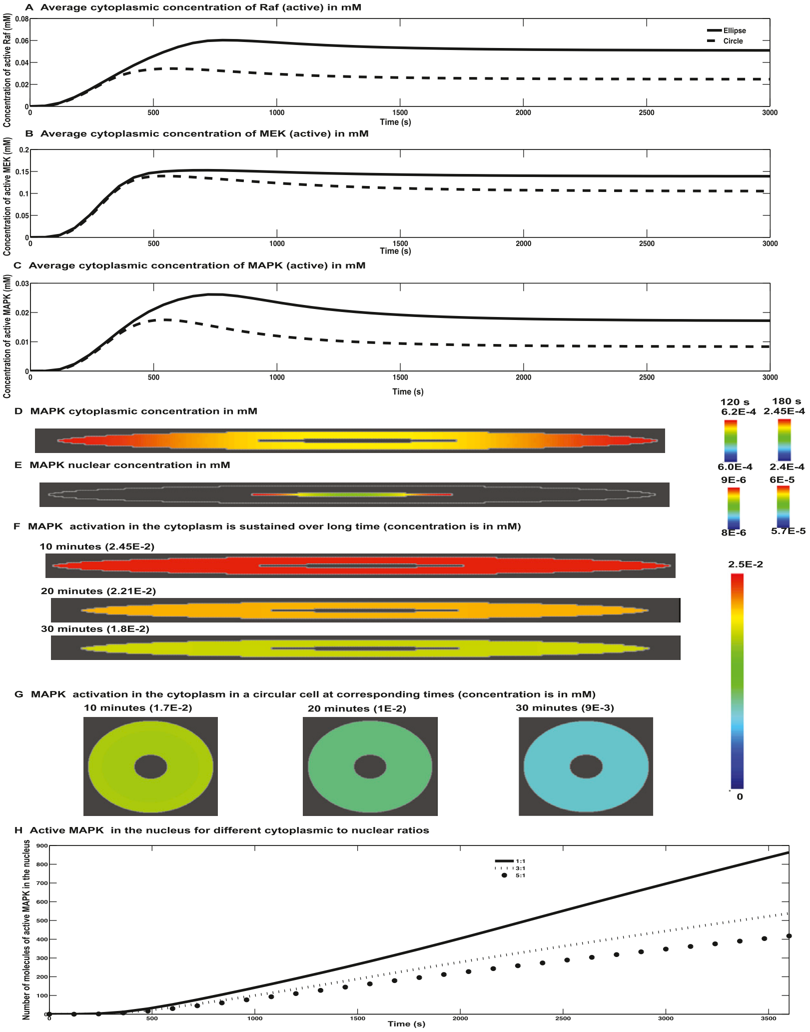

Figure S4. Flow of Signal through Raf and MEK to MAP Kinase in the Cytoplasm, Related to Figure 5

(A–C) Spatial average of the cytoplasmic concentrations of activated forms of (A) Raf, (B) MEK and (C) MAP kinase from the numerical simulations are shown as a function of time. The elliptical cell shape has a larger average concentration of Raf than a circle at earlier time points. This difference in concentration is maintained for the active MEK and MAP kinase concentrations.

(D) MAPK concentration gradients in the cytoplasm and nucleus from numerical simulations are shown at early and late times. Cytoplasmic MAPK gradient is shown for 120 s and 180 s. Active MAPK is large in regions of high curvature. As active MAPK is transferred to the nucleus, there is a depletion of cytoplasmic MAPK concentration near the nuclear boundary. However, the concentration gradients are small, because MAPK diffuses rapidly in the cytoplasm.

(E) Nuclear concentration gradient of MAPK is shown at 120 and 180 s. The spatial gradient follows the curvature dependent gradient similar to the cytoplasmic MAPK gradient.

(F) MAPK activation is sustained over long time periods in the cytoplasm. Active MAPK concentration is shown for 10, 20 and 30 min. Because the diffusivity of MAPK is large, it is hard to visualize a spatial gradient in the cytoplasm at later times, but it can be seen that the cytoplasmic gradients are minimal.

(G) The activation of cytoplasmic MAPK is shown in the circular cell shape at 10, 20 and 30 min. The numerical value of the cytoplasmic concentration is shown in parentheses next to the time point.

(H) Effect of varying cytoplasmic to nuclear volume ratio on MAPK accumulation in the nucleus. We varied the ratio of cytoplasmic to nuclear volume with both cytoplasmic and nuclear eccentricities maintained as 0.999. Decreasing the nuclear volume (increasing the ratio of cytoplasmic to nuclear volume) reduces the number of molecules of active molecules of MAP kinase that are present in the nucleus. This is because the volume of the nucleus is smaller and therefore, fewer molecules will be present.

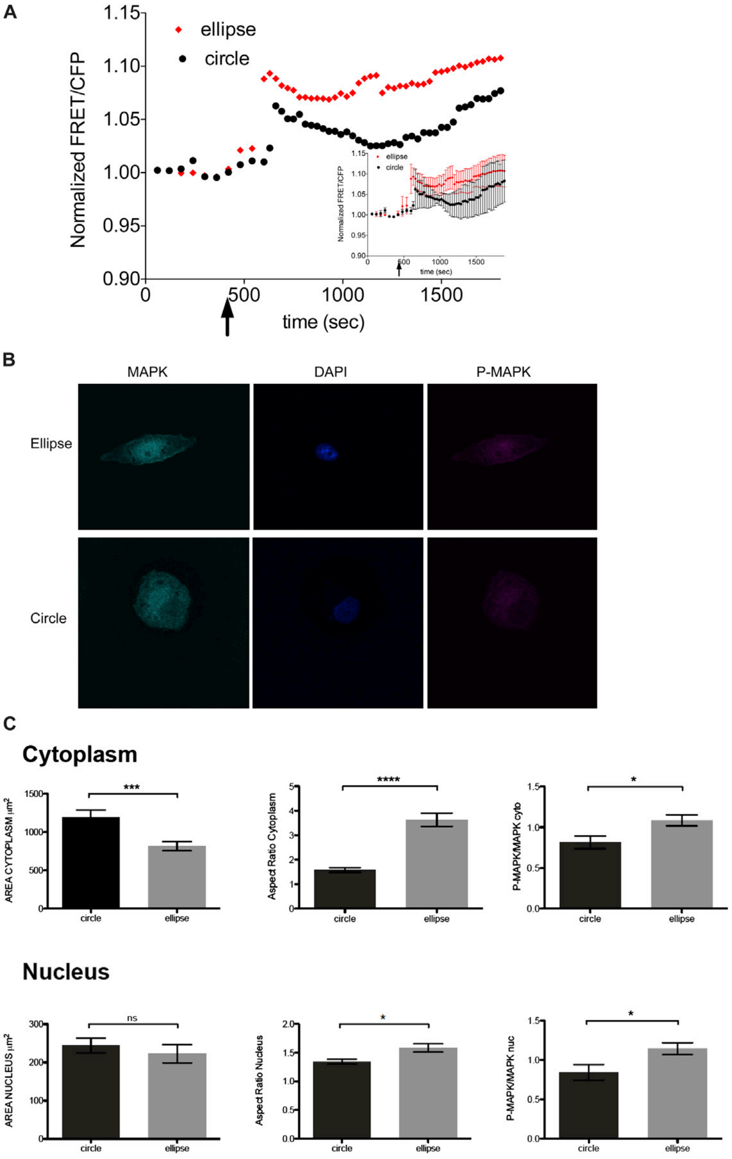

Figure S5. Live-Cell Imaging of EGFR-Induced Nuclear MAPK Activity, Related to Figure 5

(A) Patterned COS7 cells overexpressing the MAPK activity FRET reporter EKAR were imaged in response to EGF (10 ng/ml) stimulation. Fluorescence intensities of FRET and CFP channels are plotted as a ratio, normalized to the baseline. The mean of multiple (3) cells from multiple individual experiments conducted on different days was plotted (Ellipse n = 3 experiments, Circle n = 2 experiments). The mean along with the SEM is plotted in the inset. (p = 0.3975; TWO-WAY ANOVA).

(B) Immunostaining of patterned cells for p-MAPK and MAPK. Patterned cells were serum starved overnight and stimulated with EGF for 20 min. Fixed cells were immunostained for p-MAPK and total MAPK and the nucleus was counter stained with Hoescht.

(C) Cell patterning does not change nuclear area. Patterned cells were serum starved overnight and stimulated with EGF for 20 min. Fixed cells were immunostained for P-MAPK and total MAPK and the nucleus was stained with Hoescht. Images were analyzed in ImageJ (NIH) by tracing the nucleus or the cell periphery. The cellular and nuclear area and corresponding aspect ratio for each cell were determined. Fluorescence intensity values for P-MAPK and MAPK were also determined. Values were plotted as mean ± SEM (*p < 0.02; ***p = 0.0008; ****p < 0.0001; t test).

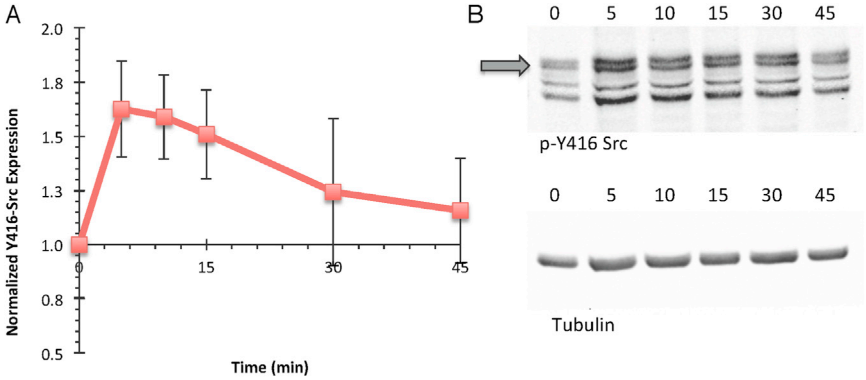

Figure S6. Experimental Measurement of Kinetic Parameters for PDGF Activation of Src, Related to Figure 6

(A) Kinetic parameters to simulate PDGF receptor signaling were constrained experimentally using an in vitro time course assay. Serum starved cardiac fibroblasts were stimulated with 10ng/ml PDGF and lysed at 0, 5, 10, 15 and 30 min post-activation. Phospho-Y416-Src (60kDa, gray arrow) levels were assessed by Western blots (B), and densitometrically quantified using ImageJ (n = 4). Data shown are mean ± SEM.